Monthly Notices of the ROYAL ASTRONOMICAL SOCIETY

MNRAS **499,** 4394–4417 (2020) doi:10.1093/mnras/staa2894
Advance Access publication 2020 September 24

ALMA observations of envelopes around first hydrostatic core candidates

María José Maureira [1,2]★ Héctor G. Arce,[1] Michael M. Dunham,[3,4] Diego Mardones,[2,5] Andrés E. Guzmán [6] Jaime E. Pineda [2] and Tyler L. Bourke[3,7]

[1]*Astronomy Department, Yale University, New Haven, CT 06511, USA*
[2]*Max-Planck-Institut für extraterrestrische Physik (MPE), Gießenbachstr. 1, D-85741 Garching, Germany*
[3]*Centre for Astrophysics | Harvard & Smithsonian, Cambridge, MA 02138, USA*
[4]*Department of Physics, State University of New York Fredonia, Fredonia, New York 14063, USA*
[5]*Departamento de Astronomía, Universidad de Chile, Casilla 36-D, Santiago, Chile*
[6]*National Astronomical Observatory of Japan, National Institutes of Natural Sciences, 2-21-1 Osawa, Mitaka, Tokyo 181-8588, Japan*
[7]*SKA Organization, Jodrell Bank, Lower Withington, Macclesfield SK11 9FT, UK*

Accepted 2020 September 16. Received 2020 September 16; in original form 2020 March 9

ABSTRACT

We present ALMA 3 mm molecular line and continuum observations with a resolution of ∼3.5 arcsec towards five first hydrostatic core (FHSC) candidates (L1451-mm, Per-bolo 58, Per-bolo 45, L1448-IRS2E, and Cha-MMS1). Our goal is to characterize their envelopes and identify the most promising sources that could be bona fide FHSCs. We identify two candidates that are consistent with an extremely young evolutionary state (L1451-mm and Cha-MMS1), with L1451-mm being the most promising FHSC candidate. Although our envelope observations cannot rule out Cha-MMS1 as an FHSC yet, the properties of its CO outflow and SED published in recent studies are in better agreement with the predictions for a young protostar. For the remaining three sources, our observations favour a pre-stellar nature for Per-bolo 45 and rule out the rest as FHSC candidates. Per-bolo 58 is fully consistent with being a Class 0, while L1448 IRS2E shows no emission of high-density tracers (NH_2D and N_2H^+) at the location of the previously identified compact continuum source, which is also undetected in our observations. Thus, we argue that there is no embedded source at the presumptive location of the FHSC candidate L1448 IRS2E. We propose instead that what was thought to be emission from the presumed L1448 IRS2E outflow corresponds to outflow emission from a nearby Class 0 system, deflected by the dense ambient material. We compare the properties of the FHSC candidates studied in this work and the literature, which shows that L1451-mm appears as possibly the youngest source with a confirmed outflow.

Key words: stars: kinematics and dynamics – stars: protostars – ISM: individual objects.

1 INTRODUCTION

Low-mass stars are born out of the gravitational collapse of dense (∼10^5 cm^{-3}) and cold (∼10 K) pre-stellar cores (Andre, Ward-Thompson & Barsony 2000). Among the most centrally condensed pre-stellar cores, there are some that might represent a stage shortly before the formation of a protostar, when the collapsing structure is predicted to harbour a compact central object known as a first hydrostatic core (FHSC; Larson 1969). Although not yet observationally confirmed, the FHSC stage, lasting up to only 10^4 yr, is routinely seen in numerical simulations of core collapse (Masunaga, Miyama & Inutsuka 1998; Saigo & Tomisaka 2006; Matsumoto & Hanawa 2011; Commerçon et al. 2012; Tomida et al. 2013; Bate, Tricco & Price 2014). The FHSC is identified as an embedded object in quasi-hydrostatic equilibrium between thermal pressure and gravity, with an initial temperature of a few 100 K and a radius of 5–20 au (Bate et al. 2014). Due to continuous accretion from the collapsing core, the central temperature and density of the FHSC increases during its lifetime. When the central region reaches a temperature of ∼2000 K, collisional dissociation of the molecular hydrogen begins, triggering a second collapse that ends with the formation of the protostar. Simulations show that the FHSC stage can play an important role on the distribution of angular momentum from the earliest stages. It is at the high densities of the FHSC object that non-ideal MHD effects can effectively remove angular momentum, impacting disc formation and early disc fragmentation (Machida, Inutsuka & Matsumoto 2014; Tsukamoto et al. 2018). Additionally, the FHSC object can launch a poorly collimated and slow (few km s^{-1}) outflow before protostar formation (Machida, Inutsuka & Matsumoto 2008; Tomida et al. 2013; Bate et al. 2014; Tomida, Okuzumi & Machida 2015, although see Price, Tricco & Bate 2012).

Observationally, a few sources have been proposed as FHSC candidates. These dense cores have extremely weak or undetected emission at wavelengths ≤70 μm, and thus are consistent with having an embedded FHSC or an extremely young (low-luminosity) Class 0 protostar (Belloche et al. 2006; Chen et al. 2010; Enoch et al. 2010; Pineda et al. 2011; Pezzuto et al. 2012). Consistent with both scenarios, follow-up interferometric observations revealed compact continuum sources and small outflows (≲few 1000 au lobe-size) at the centre of these cores (Chen et al. 2010; Dunham et al. 2011; Pineda et al. 2011; Hirano & Liu 2014; Gerin et al. 2015; Fujishiro et al. 2020). A few more candidates have been proposed based on

★ E-mail: maureira@mpe.mpg.de

Table 1. Properties of the sample of FHSC candidates observed with ALMA.

Source	M_{core}($M_\odot$)	L_{int}($L_\odot$)	24 μm ? [a]	CO_{out} lobe length[b] (au)	CO_{out} velocity[b] (km s^{-1})	Distance (pc)	Ref.
L1448 IRS2E	2.3	<0.035	No	1114	25	290	1
Per-bolo 45	2.1	<0.021	No	–	–	290	2
Per-bolo 58	0.7	0.020	Yes	7192	3	290	3
L1451-mm	0.3	<0.021	No	638	1	290	4
Cha-MMS1	0.6	0.021	Yes	2470	2–12	190	5

Notes: (1) Chen et al. (2010); (2) Kirk, Johnstone & Di Francesco (2006); Sadavoy et al. (2010); (3) Dunham et al. (2011); (4) Pineda et al. (2011); (5) Belloche et al. (2006); Busch et al. (2020).
[a]Indicates whether the source has been detected at 24 μm by *Spitzer* observations.
[b]Not corrected for inclination.

their SED alone (Young et al. 2018) and/or their compact appearance in interferometric observations of the dust emission (Schnee et al. 2012; Friesen et al. 2018). For most of these new candidates, the presence or absence of small outflows have yet to be determined. The most intriguing cases are recently reported in Friesen et al. (2018). They show two 1.3 mm compact sources (N6-mm and SM1N) at a resolution of ∼100 au, with no clear signs of an outflow. The lack of a clear outflow signature at these scales is consistent with recent theoretical predictions of the FHSC stage (Young et al. 2019).

Although both, weak or non-detected infrared emission along with compact dust and outflow detections are useful to identify candidates, they are not sufficient for identifying the youngest and most promising FHSC candidates. Molecular lines revealing the chemical and physical stage of the envelope surrounding these sources are important for identifying the candidates most likely to be bona fide FHSC. For instance, if the source is truly a young cold FHSC, or a recently born protostar, the dense collapsing envelope (disc and pseudo-disc, if present) should show no signs of warm (>20–30 K) gas/dust for which the chemistry changes due to CO desorption (Lee, Bergin & Evans 2004), at scales larger than about 100 au (Hincelin et al. 2013, 2016; Machida 2014). Similarly, the kinematics of the lines close to the centre of the core should show infall and/or rotational motions in agreement with a central compact object with a very low mass ($\lesssim$0.1 $M_\odot$).

Interferometric molecular line emission and kinematic studies have been carried out towards a few FHSC candidates. In Maureira et al. (2017a, b), we studied the candidates L1451-mm and Per-bolo 58 at 1000 au scales and found that they are indeed consistent with being in an extremely young evolutionary stage, either early Class 0 or FHSC. Similar results were obtained in Fuente et al. (2017) for the FHSC candidates in the B1b core. More recently, Marcelino et al. (2018) found evidence of a warm inner envelope (60 K at ∼200 au) and hot corino (200 K at ∼100 au) towards the southern candidate in B1b (B1b-S), and thus, this source (which had been previously designated a FHSC candidate) is now confirmed as a young Class 0 protostar. On the other hand, no such hot corino signature was found towards the northern source in this system (B1b-N, also previously designated an FHSC candidate) but high outflow velocities of up to 8 km s^{-1} have been revealed in new higher resolution (60 au) methanol observations (Hirano 2019), and is now confirmed as another very young Class 0 protostar.

In this work, we present ALMA 3 mm molecular lines and continuum observations towards five FHSC candidates at 3.5–4 arcsec resolution. Our goal is to further constrain the evolutionary state of these candidates by using the dust and dense gas distribution and kinematics at inner envelope scales. Based on these observations, we rule-out two candidates (L1448 IRS 2E, Per-bolo 58) and a third one shows strong evidence of being truly pre-stellar (Per-bolo 45). Finally, we identify one (L1451-mm) as a promising FHSC candidate for follow-up studies at high resolution.

The paper is organized as follows. In Section 2, we describe the sample and observations used in these work. In Section 3, we present our results. In Section 4, we analyse and discuss in detail the individual sources. In Section 5, we discuss the properties of the current and former FHSC candidates in this work and the literature. We also discuss future observations that can help to find new FHSC candidates as well as future high-resolution observations that can serve to confirm the true nature of the most promising targets. Section 6 corresponds to the summary and conclusions.

2 DATA

2.1 The sample

The sample of sources targeted by our ALMA observations included all FHSC candidates proposed in the literature up to the year 2012 (when ALMA Cycle 1 proposals were due) that are observable by this southern facility. This corresponded to five sources: L1448 IRS2E, Per-bolo 45, Per-bolo 58, L1451-mm, and Cha-MMS1.

The observed sources in this study are very low luminosity objects (<0.01−0.1 $L_\odot$). Only two have been detected at 24 and 70 μm (Per-bolo 58 and Cha-MMS1), with fluxes comparable to the upper limits of the remaining undetected candidates. All five sources have been associated with a far-IR/sub-mm core in low-resolution (single-dish) observation as well as with a compact sub-mm/mm continuum source in interferometric observations. Interferometric CO line observations revealed an associated molecular outflow in L1448 IRS2E (Chen et al. 2010), Per-bolo 58 (Dunham et al. 2011), L1451-mm (Pineda et al. 2011), and Cha-MMS1 (Busch et al. 2020), while in Per-bolo 45 there is no clear outflow detection (Schnee et al. 2012; Stephens et al. 2019).

Table 1 lists general properties of the sample of FHSC candidates observed with our ALMA cycle 1 observation. We have updated the values of the properties that depend on the distance to the source (core mass, internal luminosity, outflow lobe length) to be consistent with the latest distance estimates to the Perseus and Chamaeleon molecular clouds. The adopted distances are 290 pc (Ortiz-León et al. 2018; Zucker et al. 2018) for the sources in Perseus (L1448 IRS2E, Per-bolo 45, Per-bolo 58, and L1451 mm) and 190 pc for Cha-MMS1 (Dzib et al. 2018; Roccatagliata et al. 2018).

2.2 Observations

Observations for all sources in our sample were conducted with the ALMA 12m array and the Atacama Compact Array (ACA). For Cha-MMS1, observations with the Total Power (TP) array were

Table 2. Maps parameters.

Source	Map	Rest frequency (GHz)	Synthesized beam	PA	rms (mJy beam^{-1})
L1448-IRS2E	$NH_2D(1_{1,1}–1_{0,1})$	85.926	5.4 arcsec × 2.8 arcsec	−32°	24
(12m + 7m)	N_2H^+(1–0)	93.173	4.2 arcsec × 3.0 arcsec	17°	24
	HCN(1–0)	88.632	5.3 arcsec × 2.7 arcsec	−33°	34
Phase centre (J2000)	$H^{13}CO^+$(1–0)	86.754	5. arcsec × 2.8 arcsec	−34°	26
$03^h25^m25\overset{s}{.}66$	HCO^+(1–0)	89.189	5.4 arcsec × 2.8 arcsec	−33°	29
$+30^d44^m56\overset{s}{.}70$	$CH_3OH(2_{0,2}–1_{0,1})$	96.741	4.1 arcsec × 2.9 arcsec	19°	24
	$CH_3OH(3_{1,3}–4_{0,4})$	107.014	3.6 arcsec × 2.6 arcsec	16°	25
	3 mm continuum	103.55	3.5 arcsec × 2.5 arcsec	16°	0.15
Per-bolo 45	$NH_2D(1_{1,1}–1_{0,1})$	85.926	5.4 arcsec × 3.8 arcsec	−32°	34
(12m + 7m)	N_2H^+(1–0)	93.173	4.2 arcsec × 3.0 arcsec	14°	21
	HCN(1–0)	88.632	5.8 arcsec × 2.7 arcsec	−33°	34
Phase centre (J2000)	$H^{13}CO^+$(1–0)	86.754	5.4 arcsec × 2.8 arcsec	−34°	26
$03^h29^m07\overset{s}{.}70$	HCO^+(1–0)	89.189	5.5 arcsec × 2.8 arcsec	−34°	29
$+31^d17^m16\overset{s}{.}80$	$CH_3OH(2_{0,2}–1_{0,1})$	96.741	4.0 arcsec × 2.8 arcsec	16°	22
	$CH_3OH(3_{1,3}–4_{0,4})$	107.014	3.6 arcsec × 2.6 arcsec	15°	24
	3 mm continuum	103.55	3.5 arcsec × 2.5 arcsec	13°	0.15
Per-bolo 58	$NH_2D(1_{1,1}–1_{0,1})$	85.926	5.5 arcsec × 2.8 arcsec	−32°	38
(12m + 7m)	N_2H^+(1–0)	93.173	4.2 arcsec × 3.0 arcsec	17°	21
	HCN(1–0)	88.632	5.4 arcsec × 2.7 arcsec	−34°	34
Phase centre (J2000)	$H^{13}CO^+$(1–0)	86.754	5.5 arcsec × 2.8 arcsec	−34°	26
$03^h29^m25\overset{s}{.}46$	HCO^+(1–0)	89.189	5.5 arcsec × 2.8 arcsec	−33°	29
$+31^d28^m15\overset{s}{.}00$	$CH_3OH(2_{0,2}–1_{0,1})$	96.741	4.1 arcsec × 2.8 arcsec	17°	22
	$CH_3OH(3_{1,3}–4_{0,4})$	107.014	3.6 arcsec × 2.6 arcsec	15°	25
	3 mm continuum	103.55	3.5 arcsec × 2.4 arcsec	14°	0.15
L1451-mm	$NH_2D(1_{1,1}–1_{0,1})$	85.926	5.4 arcsec × 2.8 arcsec	−33°	34
(12m + 7m)	N_2H^+(1–0)	93.173	4.1 arcsec × 3.0 arcsec	16°	20
	HCN(1–0)	88.632	5.3 arcsec × 2.7 arcsec	−34°	34
Phase centre (J2000)	$H^{13}CO^+$(1–0)	86.754	5.4 arcsec × 2.8 arcsec	−34°	26
$03^h25^m10\overset{s}{.}21$	HCO^+(1–0)	89.189	5.4 arcsec × 2.8 arcsec	−34°	29
$30^h23^m55\overset{s}{.}30$	$CH_3OH(2_{0,2}–1_{0,1})$	96.741	4.0 arcsec × 2.8 arcsec	17°	21
	$CH_3OH(3_{1,3}–4_{0,4})$	107.014	3.6 arcsec × 2.6 arcsec	14°	25
	3 mm continuum	103.55	3.5 arcsec × 2.5 arcsec	14°	0.14
Cha-MMS1	$NH_2D(1_{1,1}–1_{0,1})$	85.926	3.1 arcsec × 1.8 arcsec	11°	14
(12m + 7m + TP)	N_2H^+(1–0)	93.173	2.8 arcsec × 1.8 arcsec	−11°	20
	HCN(1–0)	88.632	3.0 arcsec × 1.8 arcsec	11°	13
Phase centre (J2000)	$H^{13}CO^+$(1–0)	86.754	3.1 arcsec × 1.8 arcsec	12°	15
$11^h06^m31\overset{s}{.}23$	HCO^+(1–0)	89.189	3.0 arcsec × 1.8 arcsec	12°	14
$-77^d23^m33\overset{s}{.}57$	$CH_3OH(2_{0,2}–1_{0,1})$	96.741	2.7 arcsec × 1.8 arcsec	−11°	22
	$CH_3OH(3_{1,3}–4_{0,4})$	107.014	2.5 arcsec × 1.6 arcsec	−10°	27
	3mm cont (12m+7m only)	103.55	2.5 arcsec × 1.6 arcsec	−7°	0.13

Notes: The rms for the molecular lines is measured using channels that are 0.1 km s^{-1} wide.

also obtained. The ALMA cycle 1 Observations with the 12m and 7m arrays were taken between December 2013 and August 2014. TP array observations were taken on 2015 April. Each source was observed using a 12m array 7-pointing mosaic and a 3-point mosaic with the 7m array. The projected baselines ranged between 7m and 1290m, resulting in a largest recoverable scale of about 60 arcsec and a resolution of 3.5–4 arcsec.

The observations (all taken under project code 2012.1.00394.S; PI: D. Mardones) included two different frequency set-ups in Band 3. One set-up consisted of four spectral windows that included the lines $NH_2D(1_{1,1}–1_{0,1})$, HCN(1–0), $H^{13}CO^+$(1–0), and HCO^+(1–0). The other set-up consisted of three windows that included the lines N_2H^+(1–0), $CH_3OH(2_{0,2}–1_{0,1})$, $CH_3OH(3_{1,3}–4_{0,4})$, and a window for continuum observations. The bandwidths for the line and continuum windows were 58.6 and 2000 MHz, respectively. The corresponding channel spacings for these windows were 30.52 KHz (∼0.1 km s^{-1}) and 31 250.00 kHz (∼88 km s^{-1}).

The Common Astronomy Software Applications (CASA) package was used for both calibration and imaging. Calibration of the raw visibility data was done using the standard reduction script provided separately for the 12m, 7m, and TP array observations. Emission-free channels in all the spectral windows were combined with the continuum band to create the continuum image, which resulted in a continuum bandwidth of 2438 MHz. Imaging of the combined 12m and 7m data was done using the task *tclean* with a Briggs robust parameter of 0.5. We used the multiscale option with a threshold for cleaning of $2–3\sigma$.

For Cha-MMS1, the combined 12m and 7m CLEANed image was combined with the TP image using the task *feather*. The size of the final synthesized beams for all maps are about 4 arcsec, which at the distance of the Perseus molecular cloud (290 pc) and the Chamaeleon I molecular cloud (190 pc) corresponds to about 1200 and 800 au, respectively. Table 2 lists the line frequencies, beam sizes and rms of the final data cubes.

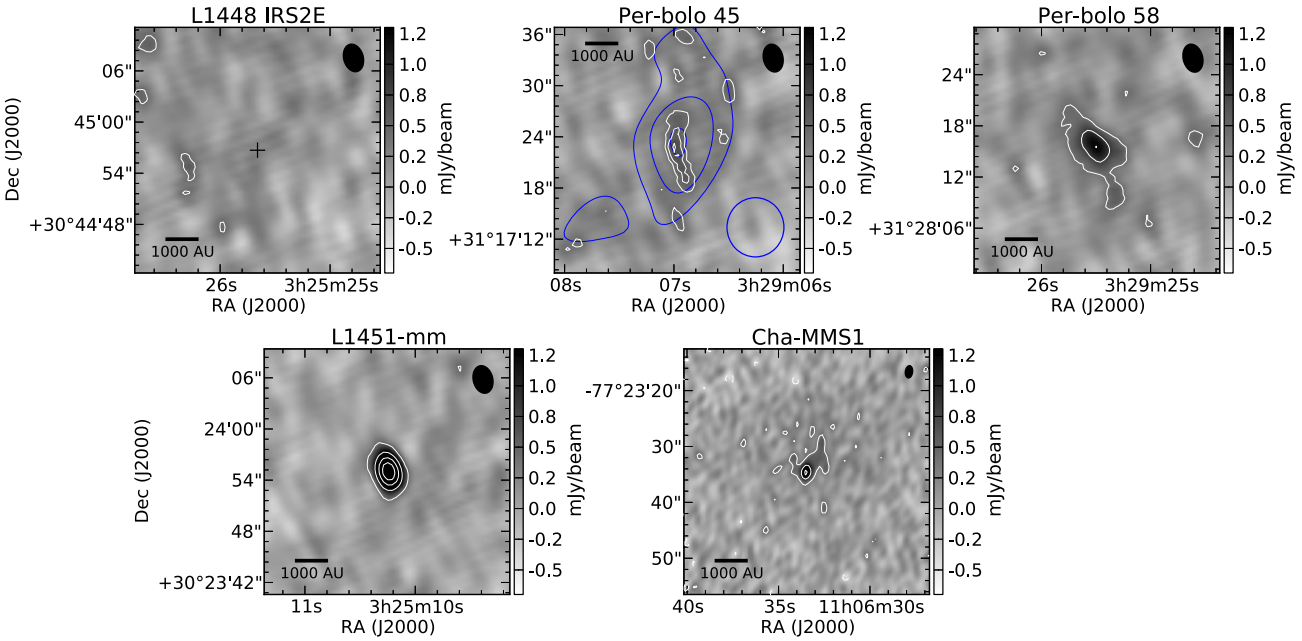

Figure 1. 3 mm continuum for all the observed sources (colour and white contours). White contours start at 3σ for all sources, and increase in steps of 1σ, 3σ, 6σ, and 6σ for Per-bolo 45, Per-bolo 58, L1451-mm, and Cha-MMS1, respectively. The location of the 1.3 mm SMA continuum peak for L1448 IRS2E (Chen et al. 2010) is marked with a cross. The synthesized beam for each map is shown in black. For Per-bolo 45, we also show the 3 mm continuum emission imaged with a beam of ∼7 arcsec (blue contours), in order to compare with previous CARMA observations of this source (Schnee et al. 2012).

2.3 ALMA archive data

We calibrated and imaged ALMA Cycle 2 (band 6) archival single pointing observations towards Cha-MMS1 (2013.1.01113.S; PI: Cordiner). We used CASA for both calibration (using the standard provided pipeline) and imaging. We used the continuum window and all available line-free channels for producing the final continuum image. We further improved the calibration by performing self-calibration on the continuum. The final image was generated with a robust parameter of 0.5, using multiscale cleaning. The final beam size, beam PA, and noise of the continuum image are 0.73 arcsec × 0.41 arcsec, −5.6°, and 0.025 mJy beam^{-1}, respectively. We applied the final self-calibration solution to the CO(2–1) and CS(5–4) line windows, and produced cubes for both lines using a robust parameter of 2, with the multiscale deconvolver option. The final beam sizes and beam PA are 0.77 arcsec × 0.51 arcsec, 0.73 arcsec × 0.49 arcsec and −33°, −32° for CO and CS, respectively. The noise, per channel, of the cubes are 5.7 and 5.5 mJy beam^{-1} for CO and CS, respectively.

3 RESULTS

3.1 3 mm continuum

Fig. 1 shows the 3 mm continuum of all the observed sources. We detected all but the FHSC candidate L1448 IRS2E. For the later, we expected a detection of at least 2σ, calculated by extrapolating the ∼6 mJy point source detection at 1.3 mm with the SMA (Chen et al. 2010), and assuming a dust opacity spectral index $\beta \approx 1.7$.

For the detected sources, Per-bolo 45 has the weakest peak flux density and also shows the less concentrated emission, which appears to be almost resolved out. The rest are point-like sources, some of them also showing extended emission.

Using CASA task *imfit*, we fit a single elliptical Gaussian component to the 3 mm continuum emission for the detected sources. This provides the position, deconvolved size, peak flux density, and total flux for each source, which are listed in Table 3. Table 4 uses these values to estimate sizes in au, masses and total gas number density. Masses from the 3 mm continuum are calculated using

$$M = \frac{d^2 S_\nu}{B_\nu(T_\mathrm{d})\kappa_\nu}, \quad (1)$$

where S_ν is the integrated flux density, B_ν is the Planck function, and κ_ν is the dust mass opacity. We assume that the dust temperature, T_d, has a value of 10 K, suitable for a pre-stellar core, or a core with a low luminosity object. We adopt a dust opacity of 0.23 cm^2 g^{-1} at 104 GHz, corresponding to an extrapolation, using $\beta = 1.7$ (Chen et al. 2016), of the 1.3 mm value in Ossenkopf & Henning (1994) for thin ice mantles after 10^5 yr of coagulation at a gas density of 10^6 cm^{-3} (so-called OH5 dust). The mass values in Table 4 are calculated assuming a gas-to-dust ratio of 100. The effective radius r_eff and total gas number density n were calculated following the convention in Dunham et al. (2016). The errors in Table 4 only consider the errors from the elliptical Gaussian fit (Table 3). Masses between 0.12 $M_\odot$ and 0.41 $M_\odot$ and densities between 1.1×10^7 and 5.4×10^8 cm^{-3} were estimated for the detected candidates. The uncertainties in the masses and thus also gas number density are larger than those reported in Table 4 (up to a factor of a few) due to the unaccounted uncertainties in the dust temperature, dust opacity, and distance. For instance, assuming a different type of dust with a higher opacity (e.g. Yen et al. 2015) would decrease the estimated masses by a factor of 2–3. Further, if we were to assume a value of β that is closer to 1 (Bracco et al. 2017), it would also increase the opacity value at 3 mm and thus would result in mass estimates that are about twice as small as our original estimate. Finally, slightly higher temperatures due to internal heating would also decrease our estimated masses. For example, a temperature of 12 K would result in mass estimates that are approximately 20 per cent lower. All these factors would result in reduction of our estimated total mass using

Table 3. Properties of continuum sources from Gaussian fit.

Source	RA (J2000)	Decl. (J2000)	Deconvolved size (arcsec)	PA deg	Peak flux density (mJy beam^{-1})	Integrated flux density (mJy)
L1448-IRS2E	–	–	–	–	<0.15	<0.15
Per-bolo 45	03:29:06.97	+31.17.22.43	(13.49 ± 3.01 , 3.40 ± 0.83)	3.2°(±4.4)	0.63 ± 0.11	4.31 ± 0.86
Per-bolo 58	03:29:25.49	+31:28:15.33	(10.05 ± 1.61 , 4.42 ± 0.73)	28.6°(±7.1)	0.95 ± 0.12	6.02 ± 0.87
L1451-mm	03:25:10.24	+30:23:55.02	point source	–	4.00 ± 0.14	4.17 ± 0.25
Cha-MMS1	11:06:33.46	−77:23:34.52	(3.15 ± 0.49 , 1.35 ± 0.42)	142°(±11)	1.74 ± 0.13	3.94 ± 0.42

Table 4. Physical properties of the dust continuum emission.

Source	Effective radius (au)	Mass ($M_\odot$)	n (cm^{-3})
L1448-IRS2E	–	<0.01	–
Per-bolo 45	982(162)	0.29(0.06)	$1.1(0.6) \times 10^7$
Per-bolo 58	966(111)	0.41(0.06)	$1.6(0.6) \times 10^7$
L1451-mm	<429	0.28(0.02)	$>1.3 \times 10^8$
Cha-MMS1	196(34)	0.12(0.01)	$5.4(3.5) \times 10^8$

Note. Values in parenthesis correspond to the uncertainties.

the 3 mm dust emission up to a factor of 6, thus in agreement with the estimates of the central object mass obtained through the gas kinematics in Section 4.

3.2 Molecular lines

Figs 2–6 show the moment 0, 1, and 2 maps for all the observed sources and molecular lines. Moment 0 maps (left column) show integration over all velocities, but only pixels with emission greater than 3σ per channel were considered. Moments 1 and 2 (middle and right columns, respectively) were calculated using the main hyperfine for $NH_2D(1_{1,1}–1_{0,1})$ and HCN(1–0), while the isolated hyperfine component was used for N_2H^+(1–0) (hence the difference in the absolute velocity shown for this line). The kinematics and emission properties of each individual source are discussed in detail in Section 4.

3.2.1 General trends in the molecular line emission

In this section, we describe general trends seen in our observed molecular lines maps, to be used later in the analysis and discussion of individual sources (Section 4).

NH_2D ($1_{1,1}–1_{0,1}$): This line is the highest density tracer in our sample. The integrated intensity of this line shows the most compact morphology for all the sources. The contour at 90 per cent of the maximum encloses the location of the continuum peak in all sources detected in the continuum, except for Cha-MMS1. In general, the emission shows a flattened morphology, with the major axis oriented perpendicular to the outflow (when present).

N_2H^+(1–0): This line has an effective excitation density of 1.5×10^4 cm^{-3} at $T = 10$ K; thus, it is also a high-density tracer. Similar to $NH_2D(1_{1,1}–1_{0,1})$, the contour at 90 per cent of the maximum of the integrated intensity encloses the location of the continuum peak in all compact sources detected in the continuum, except for Cha-MMS1. However, for these sources the morphology of the emission does not trace the same flattened morphology as the $NH_2D(1_{1,1}–1_{0,1})$. This seems to indicate that the $NH_2D(1_{1,1}–1_{0,1})$ is a better tracer of the flattened inner envelope region compared to N_2H^+(1–0).

$H^{13}CO^+$(1–0): This line is the most optically thin among the intermediate to low gas density tracers of the envelope in our sample ($H^{13}CO^+$, HCN, and HCO^+). The emission is generally weak and does not show a prominent peak near or around the continuum location in all cases, except for Per-bolo 58.

HCN(1–0), HCO^+(1–0), CH_3OH ($2_{0,2}–1_{0,1}$): These lines trace envelope, outflow material and/or envelope outflow interactions with no clear trends in their emission distribution.

4 ANALYSIS AND DISCUSSION OF INDIVIDUAL SOURCES

In the following, we discuss previous observations as well as our results and interpretation of the molecular emission towards each of the candidates.

4.1 L1448 IRS2E: star-forming core or dense gas interacting with neighbouring outflow?

L1448 IRS2E, located in the L1448 region in Perseus, was proposed as an FHSC candidate by Chen et al. (2010). This was based on the detection of an unresolved 1.3 mm continuum source with SMA observations at a resolution of ∼1000 au, located at the northern end of a high-velocity CO(2–1) jet-like structure. The presumed outflow emission extends ∼9000 au to the south, and it is only seen at red-shifted velocities (dashed magenta line in Fig. 2).

Our observations in Fig. 2 show that the 1.3 mm SMA point source lies near the northern cavity wall of the outflow driven by the nearby Class 0 system L1448 IRS2. Additionally, the red-shifted lobe of the FHSC candidate, as proposed in Chen et al. (2010), is inside the cavity of the red-shifted outflow from L1448 IRS2.

Many of the trends seen in the line emission maps in the other sources discussed in section 3.2.1 are not seen towards this FHSC candidate. For instance, there is no $NH_2D(1_{1,1}–1_{0,1})$ emission surrounding the location of the 1.3 mm SMA point source; instead, this line traces a clump located 6000 au north-east of the proposed candidate location. Close to the proposed location of this candidate, the N_2H^+(1–0) traces a narrow and elongated structure that frames the eastern side of the CO red-shifted emission observed by Chen et al. (2010) that was proposed as the first core candidate's outflow.

The HCN(1–0), HCO^+(1–0), and $CH_3OH(2_{0,2}–1_{0,1})$ integrated intensity maps peak in a compact clump, located ∼5000 au east of the 1.3 mm SMA compact source. The location of this clump is coincident with the region where the northern edge (cavity wall) of the neighboring L1448 IRS2 outflow appears to be interacting with the surrounding dense gas. The $CH_3OH(2_{0,2}–1_{0,1})$ spectrum averaged over this region shows a line with a sharp edge at the systemic velocity measured at the presumed location of the candidate ($v = 3.8$ km s^{-1}) followed by relatively bright red-shifted emission extending more than 10 km s^{-1} from the systemic velocity (see Fig. 7). This type of line is typically seen towards shocked regions

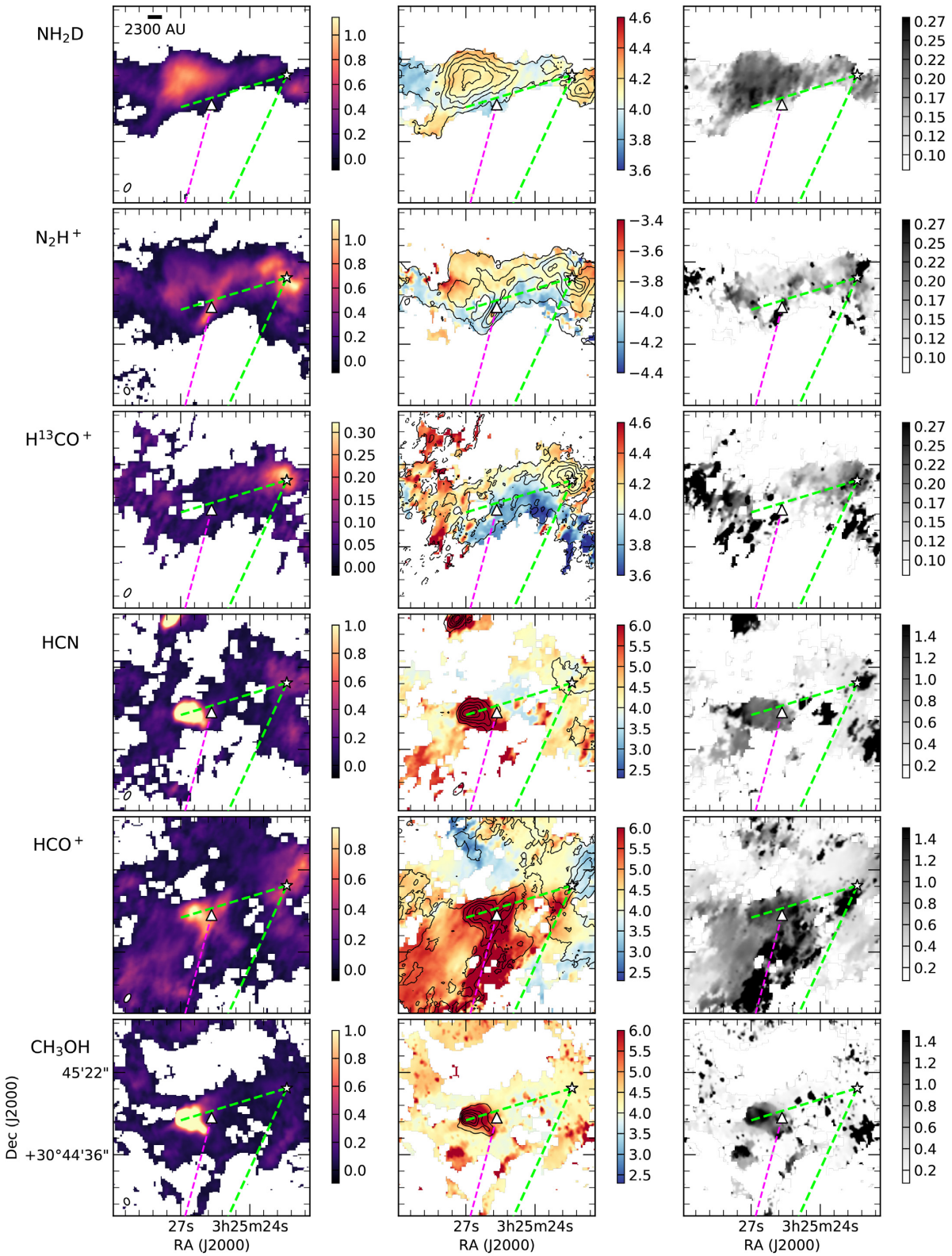

Figure 2. L1448 IRS2E: Moment 0 (left), moment 1 (middle), and moment 2 (right) maps for all the molecules with detected emission. The dashed green lines mark the positions of the cavity walls of the outflow driven by the nearby L1448 IRS2 (Class 0) protostar. The magenta dashed line marks the direction of the red-shifted outflow lobe from L144 IRS2E proposed by Chen et al. (2010). The positions of L1448 IRS2E and L1448 IRS2 are marked with a white triangle and a white star symbols, respectively. Black contours following the moment 0 are overlaid on the moment 1 map (middle). Contours start at 10 per cent of the maximum and increase in steps of 20 per cent. Colour bars are in units of Jy beam^{-1} km s^{-1}, km s^{-1}, and km s^{-1} for moment 0, 1, and 2, respectively. For each molecule, the synthesized beam is shown as a black ellipse (filled-in white) at the lower left corner of the moment 0 panel.

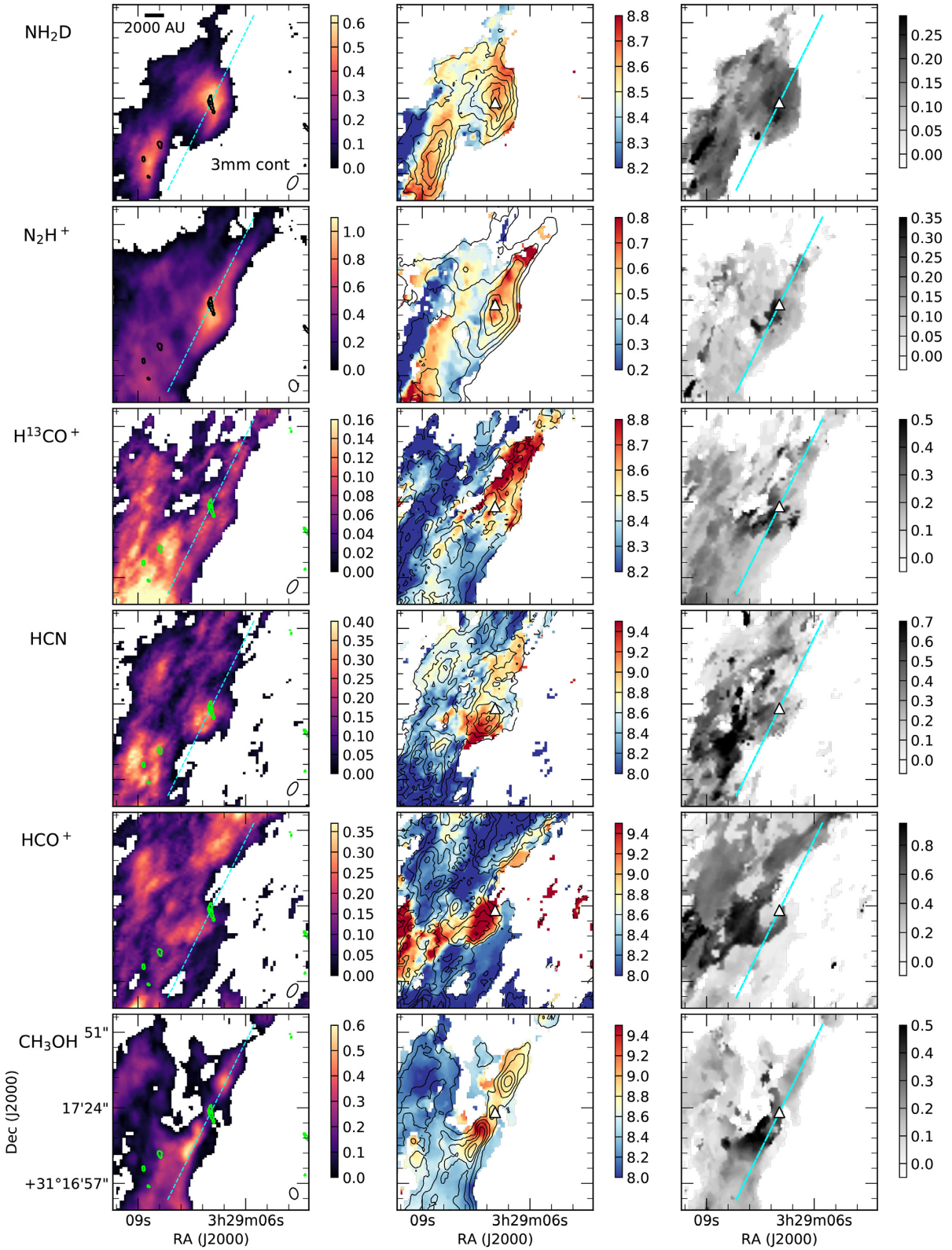

Figure 3. Per-bolo 45: Similar to Fig. 2, but for Per-bolo 45. The 3 mm continuum is shown in black/green contours on the moment 0, while the peak continuum emission is marked with a white triangle in the moment 1 and 2 columns. The cyan dashed-line shows the direction of the position–velocity cut in Fig. 8.

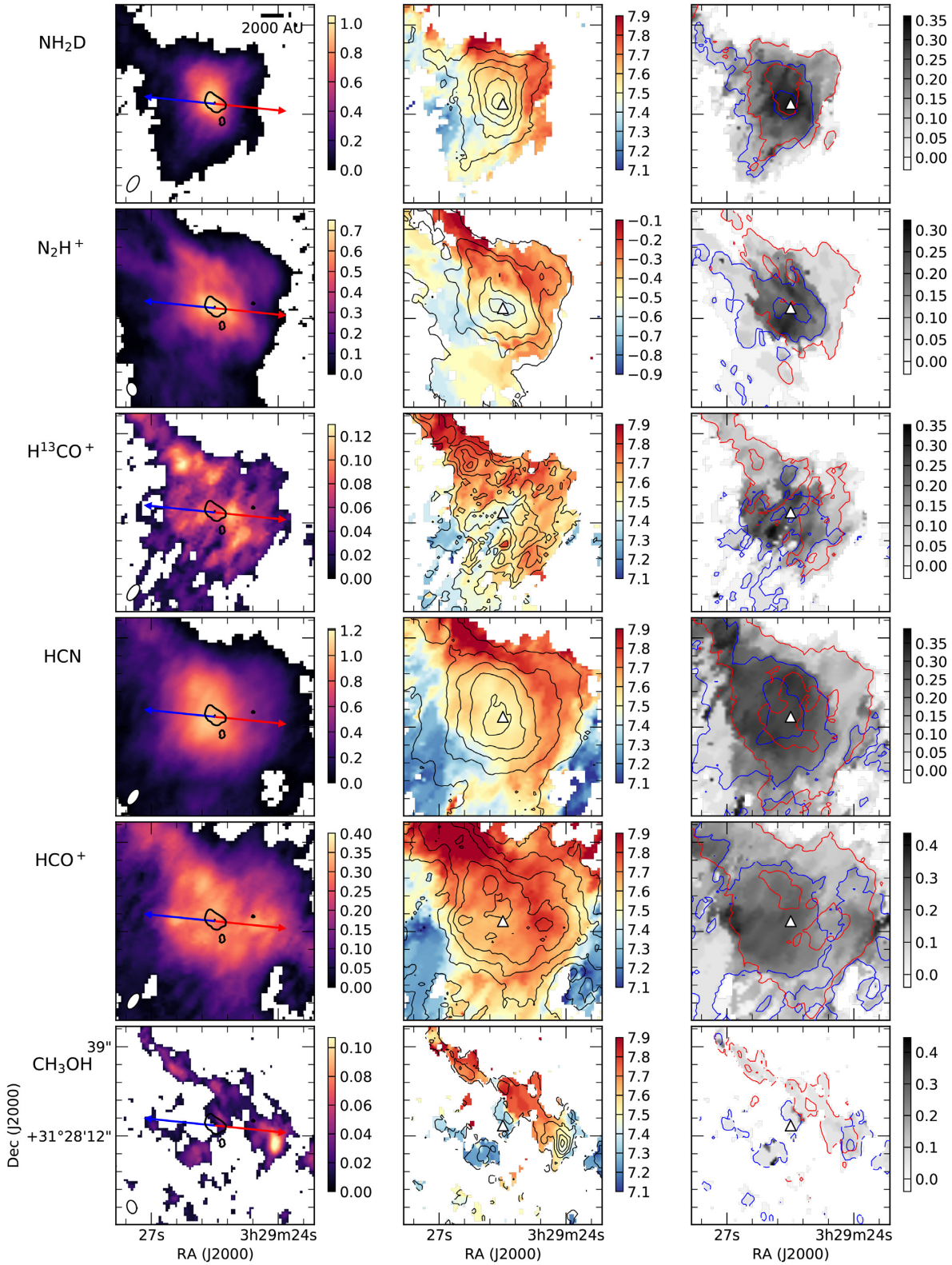

Figure 4. Per-bolo 58: Similar to Fig. 2, but for Per-bolo 58. The 3 mm continuum is shown in black contours on the moment 0, while the peak is marked with a white triangle in the moment 1 and 2 maps (middle and right columns, respectively). Red and blue contours on the moment 2 (right) show the integrated intensity of the blue velocity component (7.1–7.5 km s^{-1}) and the red velocity component (7.6–8.1 km s^{-1}), corresponding to the two distinct velocity components seen in the spectra (Fig. A3). Blue and red contours are plot at the 20 per cent and 80 per cent of the maximum. The blue and red arrow show the direction and extent of the blue and red lobe of this source's outflow.

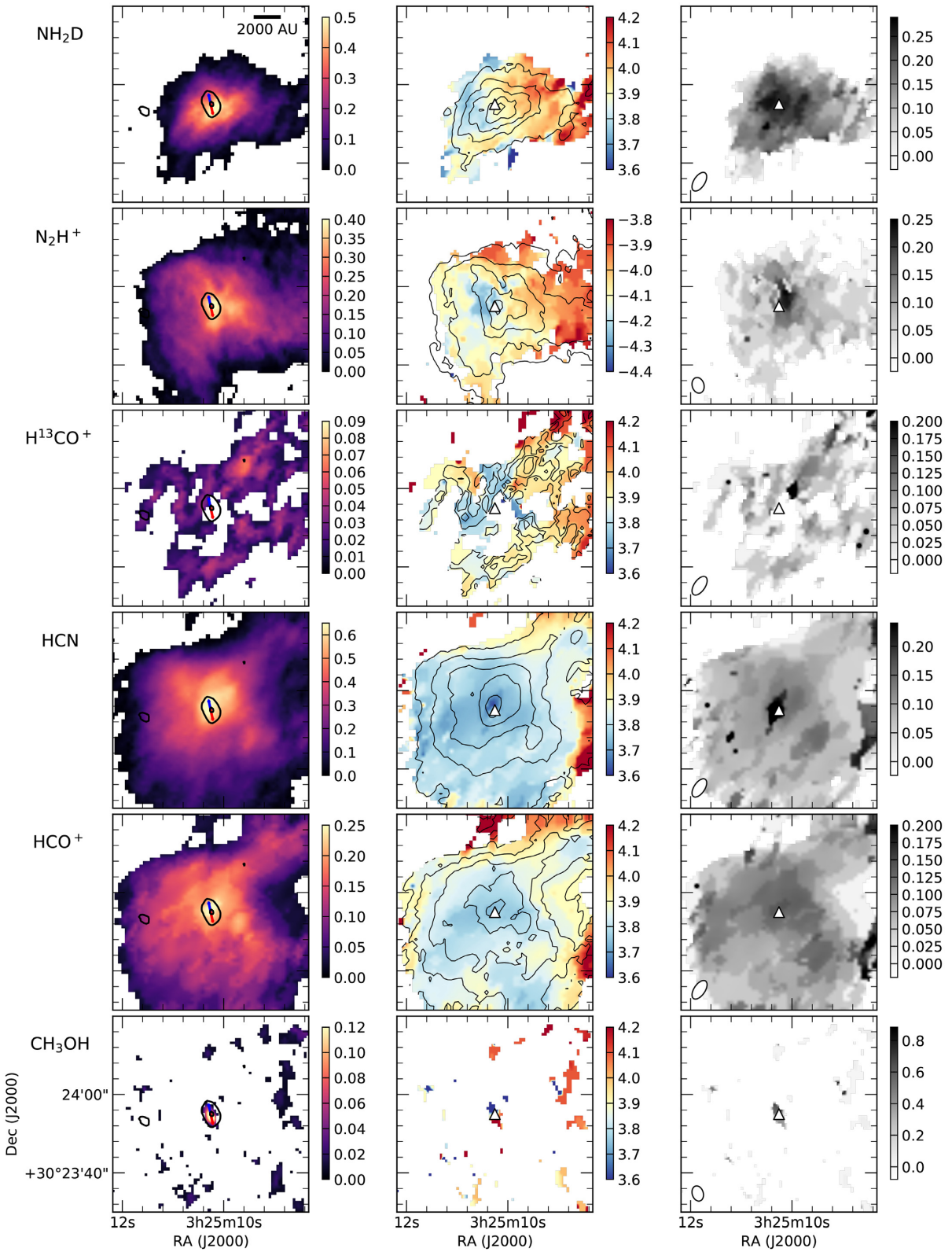

Figure 5. L1451-mm. Similar to Fig. 2, but for L1451-mm. The 3 mm continuum is shown in black contours on the moment 0, while the peak is marked with a white triangle in the moment 1 and 2 maps, in the middle and right columns, respectively. The blue and red arrows show the direction and extent of the blue and red lobe of this source's outflow.

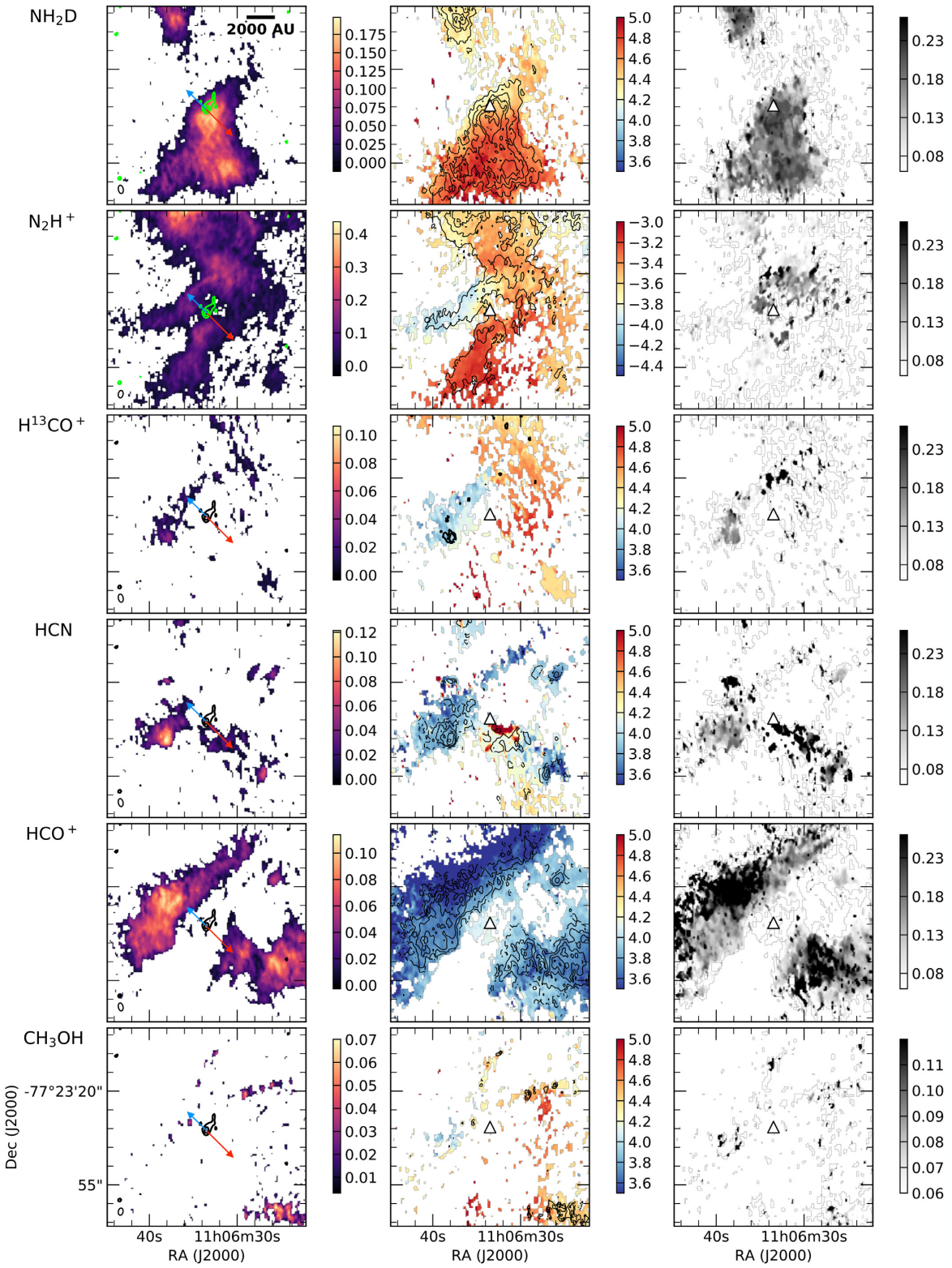

Figure 6. Cha-MMS1. Similar to Fig. 2, but for Cha-MMS1. The 3 mm continuum is shown in black/green contours on the moment 0 maps (starting at 4σ and increasing in steps of 6σ), while the peak is marked with a white triangle in the moment 1 and 2 maps (middle and right columns, respectively). The blue and red arrow show the direction and approximate extent of the blue and red lobes of this source's outflow. These maps have not been combined with the Total Power data (see Fig. 12 for the final combined 12m+7m+TP maps).

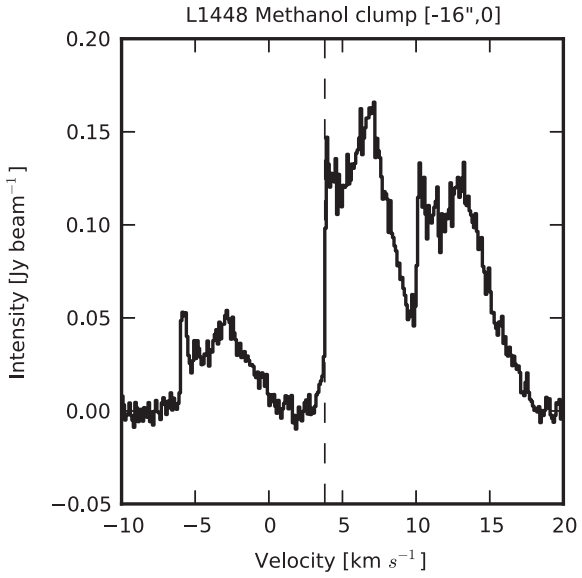

Figure 7. $CH_3OH(2_{0,2}–1_{0,1})$ spectrum towards the bright clump to the east of the L1448 IRS2E candidate location. The spectrum is averaged over a circle with radius 10 arcsec, enclosing most of the clump. This type of broad line showing a sharp edge and an extended tail of high velocities is typical of shocked regions. The vertical line corresponds to $v = 3.8$ km s^{-1}, the systemic velocity at the location of the candidate (see spectra Fig. A1).

impacted by protostellar outflows (Suutarinen et al. 2014). Similar wide velocity profiles are seen towards this clump in HCN(1–0) and HCO^+(1–0). In addition, the velocity range of this gas is consistent with the velocity range of the red-shifted outflow lobe from L1448 IRS2 (Chen et al. 2010).

Our observations thus indicate a lack of concentrated emission from high-density tracers at the location of the proposed candidate, along with evidence of the impact of the neighboring L1448 IRS2 outflow near the presumed first core candidate location, traced by low-density and shock gas tracers. Based on these, and the lack of detection of a 3 mm continuum point source in our ALMA observations, we propose that the red-shifted emission interpreted as outflow from a FHSC candidate by Chen et al. (2010) is emission from the outflow from the nearby Class 0 system L1448 IRS2 that has been deflected by the dense gas present at the location where L1448 IRS2E was thought to be. Thus, we believe that there is no star-forming core at this location and rule-out L1448 IRS2E as an FHSC. This interpretation is also consistent with the recently reported non-detection of 1.3 mm continuum emission in the SMA observations with a resolution of 300 au, as part of the MASSES survey (Stephens et al. 2019). Those observations had enough sensitivity to detect the ∼6 mJy point source from Chen et al. (2010) with a significance of 8σ.

4.2 Per-bolo 45: a prestellar core?

Per-bolo 45 is a bound dense Far-IR/sub-mm core (Enoch et al. 2008) located in the Perseus NGC 1333 cluster region, in between IRAS 7 to the north-east and SVS 13 to the southwest. Single-dish observations (with an FWHM resolution of 30 arcsec), along with *Spitzer* observations were used to classify Per-bolo 45 as a starless core (Enoch et al. 2008). Subsequent interferometer observations with a resolution of ∼7 arcsec lead Schnee et al. (2012) to propose this source as an FHSC candidate. Their observations detected a compact (∼3300 au) continuum source with molecular lines showing broader linewidths towards the centre. In addition, they detected extended SiO(2–1) emission, 20 arcsec south from the continuum source, with an elongated morphology somewhat reminiscent of an outflow (yet with velocities within 1 km s^{-1} of the ambient velocity). They interpreted these results as tentative evidence for an outflow and concluded that Per-Bolo 45 might already had formed a compact central object, such as FHSC or a young protostar.

In our observations, the $NH_2D(1_{1,1}–1_{0,1})$ and N_2H^+(1–0) emission concentrate around the weak continuum emission. On the other hand, the $H^{13}CO^+$(1–0) shows lower emission at the position of the continuum source, within a region with a size of ∼1000 au, which could be explained by freeze-out of carbon-bearing molecules (Lee et al. 2004; Bergin & Tafalla 2007). These features are consistent with a dense core in a young evolutionary stage (pre-stellar to young Class 0 protostar). Yet, the weak elongated dust structure at 1000 au scales (Fig. 1) is more consistent with what one would expect for a pre-stellar (or starless) core (Dunham et al. 2016). To further favour or reject the pre-stellar nature of this core, we investigate whether our observations support the presence of an outflow.

4.2.1 *Searching for an outflow powered by Per-bolo 45*

Consistent with the observations in Schnee et al. (2012), Fig. 2 shows that the emission and linewidths of the $CH_3OH(2_{0,2}–1_{0,1})$, HCO^+(1–0), and HCN(1–0) lines indeed suggest that this source might have an outflow. They show an elongated structure at red-shifted velocities to the south of the FHSC candidate with a corresponding broadening of the lines. The SiO(2–1) detected in Schnee et al. (2012) is about 10 arcsec south from Per-bolo 45 and is oriented along the same direction as our observed $CH_3OH(2_{0,2}–1_{0,1})$ emission, at similar velocities. Yet, the velocity of these features remains within ∼1.5 km s^{-1} from the source systemic velocity; i.e. they do not trace truly high-velocity gas.

We made position–velocity diagrams of these lines to investigate if these features could correspond to a low-velocity outflow. Fig. 8 shows position–velocity maps of HCO^+(1–0), HCN(1–0), and $CH_3OH(2_{0,2}–1_{0,1})$, along a cut aligned with the two peaks of the $CH_3OH(2_{0,2}–1_{0,1})$, and passing through the continuum peak of Per-bolo 45 (cyan dashed line in Fig. 3). A red-shifted feature, about 1.4 km s^{-1} away from the cloud velocity (8.6 km s^{-1}), is observed in all lines except for $H^{13}CO^+$(1–0). However, the lack of corresponding blue-shifted feature and the low-velocity and morphology of this red-shifted feature prevent us from concluding that this could be associated with an outflow from Per-bolo 45 rather than, for example infall. Consistent with this, no clear outflow is detected in the CO(2–1) observations of the MASSES survey Stephens et al. (2018, 2019). Their CO(2–1) map shows a red-shifted feature to the south and west of the continuum source, surrounding the structure traced by $NH_2D(1_{1,1}–1_{0,1})$ and N_2H^+(1–0). This emission was proposed by Plunkett et al. (2013) as the tip of a red-shifted outflow lobe from the source SVS 13c, located 180 arcsec (∼0.2 pc) to the southwest of Per-bolo 45. The interaction of this outflow with Per-bolo 45 dense core would provide a natural explanation to some of the higher velocity emission seen in the maps of HCO^+(1–0), HCN(1–0), and $CH_3OH(2_{0,2}–1_{0,1})$, as well as to the SiO emission (Jiménez-Serra et al. 2010) that was observed in Schnee et al. (2012).

The properties of the continuum emission and the dense gas tracers in our sample, as well as the lack of conclusive evidence of an outflow strongly suggest that Per-bolo 45 is pre-stellar in nature, not having formed a compact object such a FHSC yet.

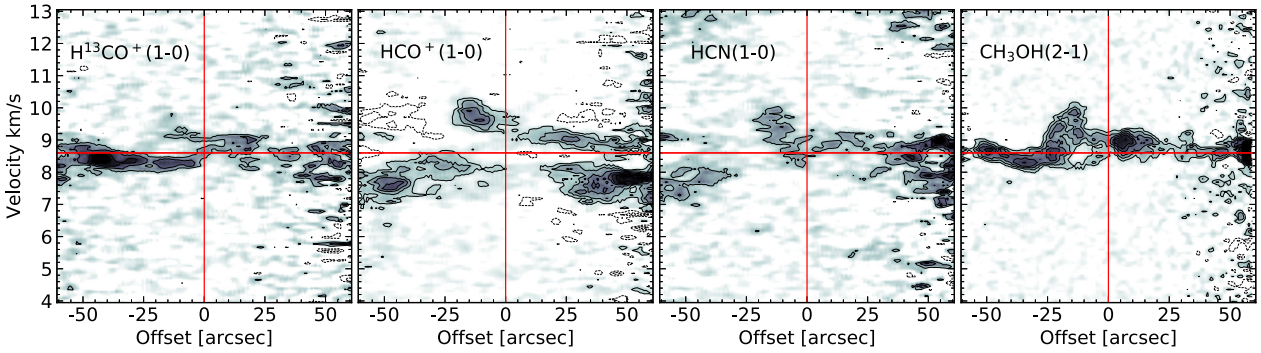

Figure 8. Per-bolo 45 position–velocity diagrams along the $CH_3OH(2_{0,2}–1_{0,1})$ elongated structure ($PA_{out} = -27°$), shown in Fig. 3. The $H^{13}CO^+$(1–0) is an envelope tracer, while the rest are used to probe outflow motions. We do not find clear evidence for an outflow driven by this candidate. Contours start at 3σ and increase in steps of 3.5σ (σ values listed in Table 2). Similar dashed contours are drawn for negative emission. Red lines mark the position of the continuum source and the source velocity $v = 8.6$ km s^{-1}.

4.3 Per-bolo 58: a young Class 0 protostar

Per-Bolo 58 is a dense Far-IR/sub-mm core located in the northern part of the NGC 1333 region in Perseus. It was identified as a FHSC candidate by Enoch et al. (2010) based on weak detections at 24 and 70 μm in *Spitzer* observations. Follow-up SMA observations at a resolution of 2.7 arcsec (∼780 au) revealed a 1.3 mm compact source and a CO(2–1) bipolar outflow (Dunham et al. 2011). The outflow appears jet-like with a characteristic projected velocity of 2.9 km s^{-1}. If the source is close to edge-on, the jet-like outflow velocity may be significantly faster, contrary to the typical properties of the FHSC outflow in simulations (Machida et al. 2008; Bate et al. 2014).

In Maureira et al. (2017b), we studied this source with 3 mm CARMA observations of molecular lines, at a resolution of 6 arcsec (NH_2D, N_2H^+,HCN, HCO^+, CS). The CARMA observations revealed line profiles with two distinct peaks separated by 0.4–0.6 km s^{-1}, arising from two different optically thin velocity components along the line of sight. These two velocity components are also present in our ALMA observations, including in the optically thin line $H^{13}CO^+$(1–0). The two velocity components spatially overlap in a region that is a few 10^3 au in size towards the centre of the core, seen as the region with significantly higher values of the line width in the moment 2 maps (see Fig. 4). In Maureira et al. (2017b), we concluded that the detected profiles with two velocity components could arise from infall motions in an in-homogeneous and flattened envelope seen close to edge-on and/or as a consequence of accretion from large-scale filamentary structures.

A unique future among our sample, Fig. 4 shows that the $H^{13}CO^+$(1–0) emission is bright close to the central region of the core. This provides independent evidence that the evolutionary stage of this source is more evolved that the FHSC phase. This is because the size of the region in which carbon-bearing molecules are 'back in' the gas phase (after being released from the dust icy mantles due to heat from the central source) increases with time (Lee et al. 2004; Jørgensen, Schöier & van Dishoeck 2005). In Per-bolo 58, this region is large enough to be detectable in our ∼1000 resolution observations.

4.3.1 Infall and rotation

Fig. 9 (top panels) shows position–velocity diagrams of the most blue-shifted satellite of the $NH_2D(1_{1,1}–1_{0,1})$ line, and the isolated hyperfine component of N_2H^+(1–0). The p–v diagrams correspond to cuts perpendicular and along the outflow. Perpendicular to the outflow, the higher intensity contours of both molecules show a hint of a velocity gradient (from the bottom-left to the upper-right quadrant). Along the outflow direction, no clear gradient is observed. However, there is an indication of higher velocity towards the centre in N_2H^+(1–0). These signatures, a gradient perpendicular to the outflow and higher velocities towards the source location, are expected when there is a combination of rotational and infalling motions (Hogerheijde 2001).

In order to estimate the mass of the central object that can produce the velocity structure observed in the p–v diagrams, we compare the position–velocity cuts with a toy model that assumes infall and rotation with conservation of angular momentum (Ulrich 1976). Here, we give a brief description of the model (for further details, see Appendix C). The free parameters are the mass of the central object and the disc radius (which is assumed to be twice the radius of the centrifugal barrier). We do not expect to reproduce the emission at every position since clearly, the envelope structure is more complex than a spherical toy model. Likewise, a caveat of this model is that it assumes that the mass of the system is dominated by the central object mass. This might not be the case for extremely young objects such an FHSC, because such a young object might have proportionately more mass in the envelope compared to central region with respect to more evolved protostars. Given this, our estimated central mass can be taken as an upper limit. On the other hand, the model does not consider velocities smaller than those expected from free-fall (for instance in the presence of magnetic fields), which nevertheless have been observed at higher resolution towards some sources (e.g. Ohashi et al. 2014) and may result in an underestimation of the central object's mass by a factor of a few (Yen et al. 2015). Despite these caveats, the model is still useful for comparing the FHSC candidates within the sample and Ulrich models applied to older objects including extremely young Class 0 protostars (Yen et al. 2013; Oya et al. 2014; Yen et al. 2015). Models are calculated for a grid of masses and disc sizes and the best model for each source and species correspond to that with the least residual between the observed and modelled position–velocity maps. The best models for NH_2D and N_2H^+ are shown in Fig. 10 in colour. They indicate values for the mass of the central object of $0.16^{+0.02}_{-0.02}$ $M_\odot$ and $0.12^{+0.04}_{-0.02}$, respectively. The disc radius of the best models range from 100 to 300 au. We note however that at the scales of our observations infall dominates over rotation and our constraint on the disc radius is poor. The value of the mass is slightly larger than what would be expected for an FHSC (≈ 0.1 $M_\odot$, Tomida et al. 2015).

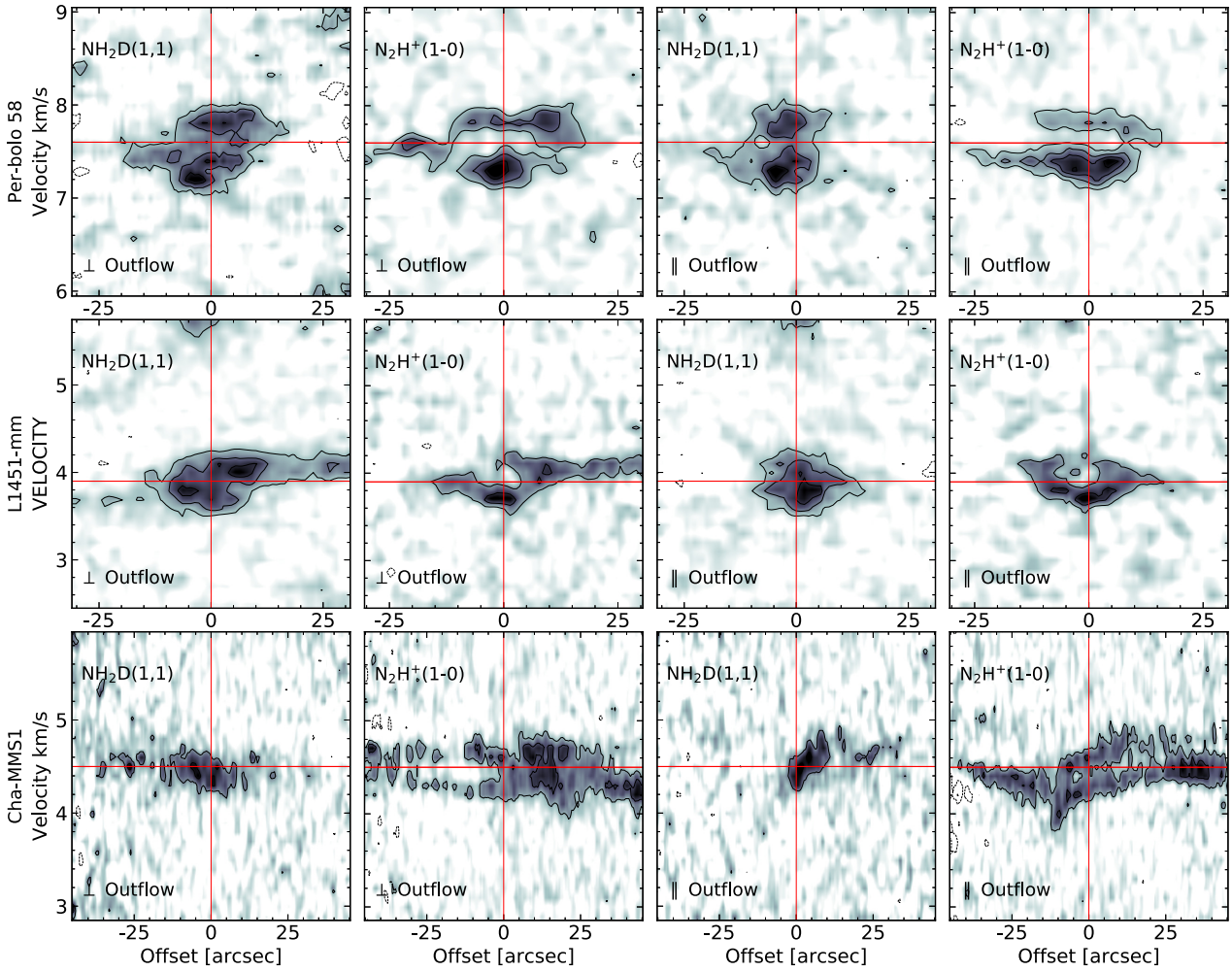

Figure 9. Per-bolo 58 (top), L1451-mm (middle), and Cha-MMS1 (bottom) position–velocity diagrams for $NH_2D(1_{1,1}–1_{0,1})$ and $N_2H^+(1–0)$, at cuts perpendicular and parallel to the outflow. For Per-bolo 58 and Cha-MMS1, the most blue-shifted hyperfine of $NH_2D(1_{1,1}–1_{0,1})$ is shown. For L1451-mm, individual satellites were weak. Hence, we show the average of the four satellites (see Appendix B). The systemic velocity is marked with a horizontal line at $v = 7.6$ km s^{-1}, $v = 3.9$ km s^{-1}, and $v = 4.5$ km s^{-1} for Per-bolo 58, L1451-mm, and Cha-MMS1, respectively. Contours start at 3σ and increase in steps of 3σ, with σ listed in Table 2 for each transition. The direction of the cuts is shown at the bottom-left corner of each panel.

4.3.2 Outflow

The outflow is clearly identified only in the HCO^+ (Fig. 11). Emission at velocities 0.5–1 km s^{-1} away from the source's systemic velocity is observed at distances $\gtrsim$3000 au from the continuum location, consistent with the ∼7000 au CO outflow lobe length observed by Dunham et al. (2011) with SMA observations. The lobe length measured in the SMA observations should also be considered a lower limit for the outflow's true extent as outflow emission is detected right up to the edges of the primary beam.

In summary, the discussed presence of brighter $H^{13}CO^+(1–0)$ emission towards the centre of this source, the extension and properties of the CO outflow (Dunham et al. 2011) and our mass estimate for Per-bolo 58 are all consistent with this source more likely being a young (Class 0) protostar rather than a FHSC.

4.4 L1451-mm: a promising FHSC candidate

L1451-mm is a dense Far-IR/sub-mm core in the quiescent dark cloud L1451 in the western end of the Perseus molecular cloud. This region appears to be in an early evolutionary state, with no *Spitzer*-identified YSOs at wavelengths shorter than 160 μm. Observations with the SMA with a resolution of 1 arcsec (∼290 au) revealed a 1.3 mm continuum point source and an unresolved, low-velocity (∼2 km s^{-1}) CO outflow. This is, to the best of our knowledge, the smallest (lobe length ∼500 au) and weakest outflow detected in a low-mass star-forming core (Dunham et al. 2011; Pineda et al. 2011).

Among all our observed lines towards L1451-mm, $H^{13}CO^+(1–0)$ is the only one that does not peak at the position of the continuum, showing a lack of emission within ∼1000 au from it. The absence of emission from this molecule towards the centre of the core suggests that carbon-bearing molecules are still frozen on to dust grains towards the centre of L1451-mm, as typically seen in pre-stellar cores (Caselli et al. 2002). This is also consistent with the non-detection of $C^{18}O$ (2–1) in SMA observations of this candidate, at a sensitivity of ∼0.3 K (Stephens et al. 2019), further supporting an extremely young evolutionary state for this object. We note that HCO^+ and HCN are significantly more abundant than $H^{13}CO^+$ and can be found in the gas state in the outer layers of cores even when these carbon-bearing species are locked in the ice in the inner cold regions of the core. Thus, $HCO^+(1–0)$ and HCN(1–0) emission from the outer layers of the core can contribute significantly to the total

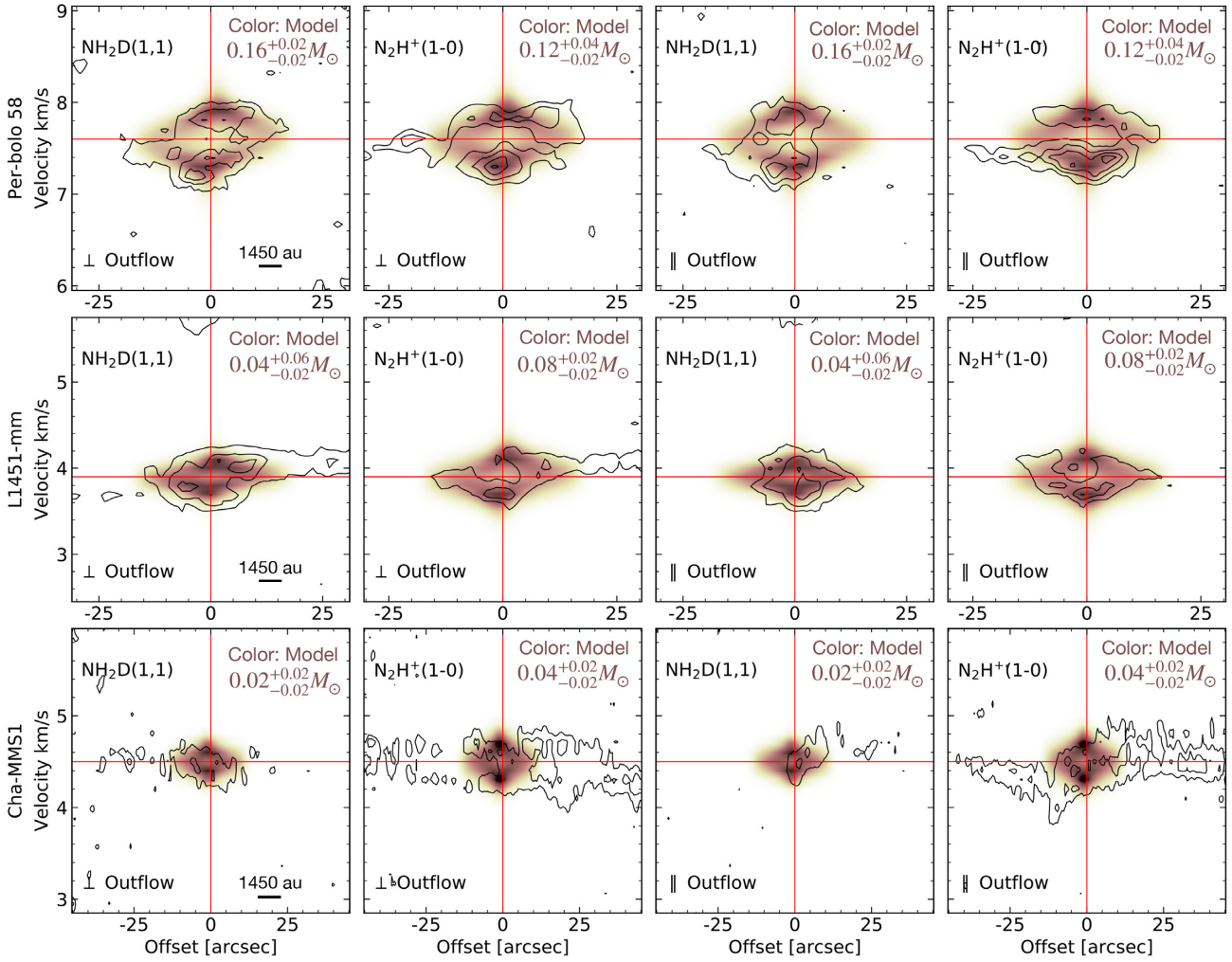

Figure 10. Position–velocity diagrams of $NH_2D(1_{1,1}–1_{0,1})$ and $N_2H^+(1–0)$(shown in black contours) of Per-bolo 58 (top), L1451-mm (middle), and Cha-MMS1 (bottom) at cuts perpendicular and parallel to the outflow of each source (same as Fig. 9). The best infalling and rotating envelope model for each source and line is shown in colour (brown-scale). The central mass inferred by the model is indicated at the upper right corner of each panel.

integrated intensity of the core map, resulting in peaks towards the centre of the moment 0 maps of these two species, while the optically thinner $H^{13}CO^+(1–0)$ shows a hole.

4.4.1 Infall and rotation

Similar to Per-bolo 58, the $NH_2D(1_{1,1}–1_{0,1})$ and $N_2H^+(1–0)$ show velocity gradients perpendicular to the outflow and higher velocities towards the centre (the middle panel of Fig. 9). We interpret these observations as evidence for rotation and infall motions. We use the same model as for Per-Bolo 58 (see Appendix C). The best model, shown in Fig. 10, results in a central mass of $0.04^{+0.06}_{-0.02}$ $M_\odot$ and $0.08^{+0.02}_{-0.02}$ $M_\odot$ using $NH_2D(1_{1,1}–1_{0,1})$ and $N_2H^+(1–0)$, respectively. The disc radius of the best models ranges from 100 to 300 au (i.e. the full range of values we explored, except from a value of 0 au, or no disc). The low-mass estimate is consistent with both an FHSC or a very young protostar. To the best of our knowledge only three protostars to date show similar low masses when their envelopes are observed at similar resolution and a similar method is used to derive their mass. These are IRAS 16253–2429: 0.03 $M_\odot$, NGC 1333 IRAS 4B: 0.07 $M_\odot$, L1157–mm: 0.05 $M_\odot$, from the Yen et al. (2015) survey that studied 17 Class 0/I sources. Most sources in that survey have masses that are greater than 0.1 $M_\odot$, similar to our estimate for Per-bolo 58. Furthermore, for these few protostellar sources with estimated masses smaller than 0.1 $M_\odot$, the $C^{18}O$ has been clearly detected at ∼700–1000 au scales (Yen et al. 2015), while for L1451 mm, it remains undetected with a resolution of ∼1000 au at comparable sensitivities (Stephens et al. 2018).

4.4.2 Outflow

Among the different lines we observed, the outflow in this source is only clearly detected in the HCN(1–0) and $CH_3OH(2_{0,2}–1_{0,1})$ maps. In these lines, a significantly larger velocity width is seen in the moment 2 maps in a region close to the continuum peak, with an approximately north–south morphology (see Fig. 5). Evidence of the existence of a very compact outflow is also seen in the p-v diagrams along the outflow axis, where red- and blue-shifted emission with velocities of up to ±1.5 km s^{-1} away from the systemic velocity is seen the HCN(1–0) and $CH_3OH(2_{0,2}–1_{0,1})$ lines close to the continuum peak position (Fig. 11). Hints of a red-shifted outflow lobe are also seen in the p–v of the $HCO^+(1–0)$ line. In all cases,

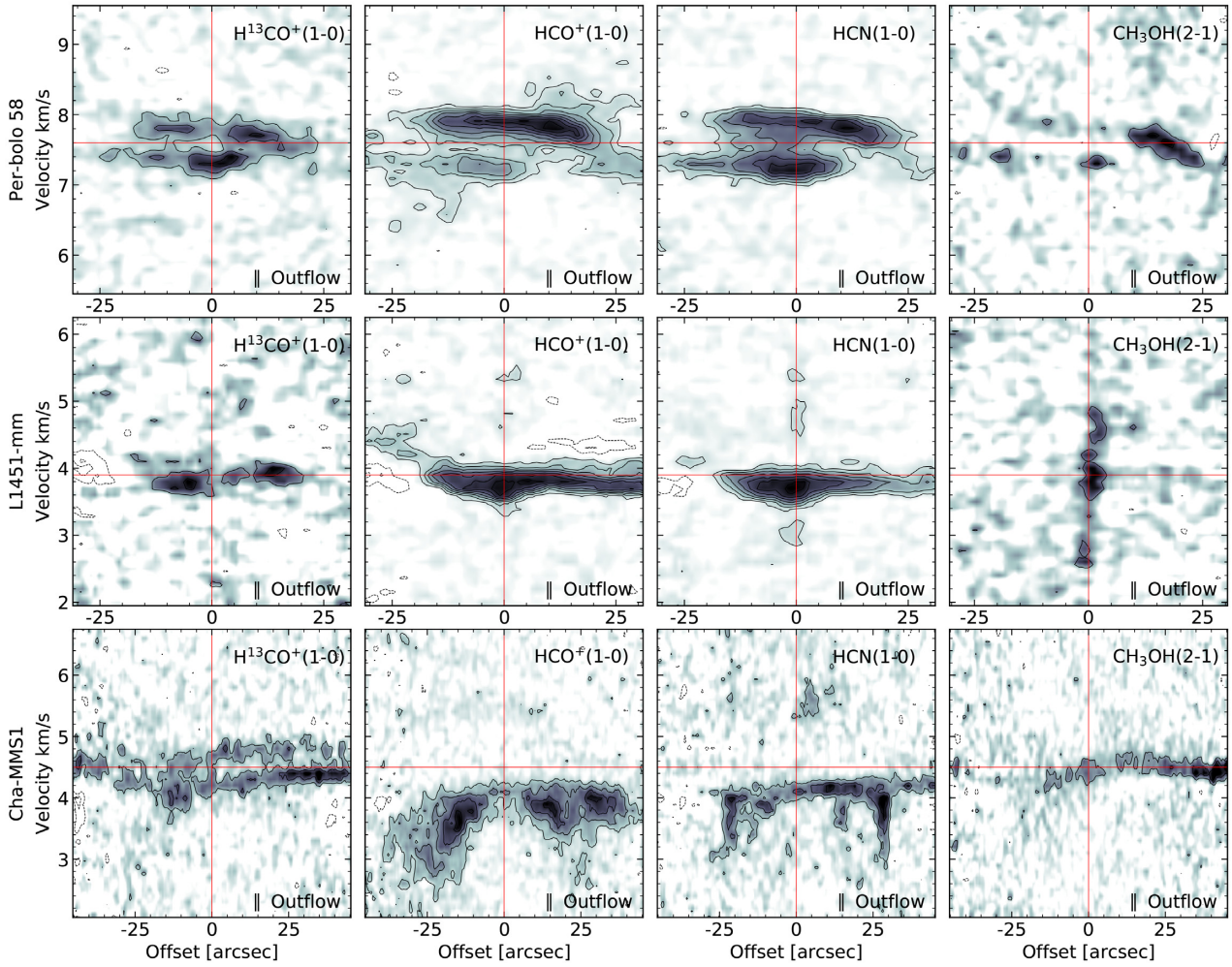

Figure 11. Per-bolo 58 (top), L1451-mm (middle), and Cha-MMS1 (bottom) position–velocity diagrams for $H^{13}CO^+$(1–0), HCO^+(1–0), HCN(1–0), and $CH_3OH(2_{0,2}–1_{0,1})$ at cuts along the outflow direction of each source. The zero offset corresponds to the position of the continuum source, listed in Table 3 and the zero velocity corresponds to the systemic velocity of the sources (7.6 , 3.9, and 4.5 km s^{-1} for Per-bolo 58, L1451-mm and Cha-MMS1, respectively). Contours start at 3σ and increase in steps of 3σ, with σ listed in Table 2.

the high-velocity emission region is restricted to within a beam from the continuum peak position ($\lesssim 10^3$ au). The size, the approximately north–south morphology, as well as the velocities of the putative outflow emission in our observations are consistent with the CO outflow in L1451 mm observed by Pineda et al. (2011).

The properties observed towards L1451-mm are extremely rare among typical Class 0 sources and suggest that it is one of the youngest (if not the youngest) known low-mass protostellar source and thus a promising FHSC candidate. Higher-resolution observations are required to further constrain the true evolutionary state of this source (discussed in Section 5).

4.5 Cha-MMS1: a young star-forming core interacting with a nearby outflow

Cha-MMS1 is a dense core in the Chamaeleon I molecular cloud in a region known as Ced 110. Belloche et al. (2006) proposed it as a FHSC candidates based on weak emission at 24 μm and 70 μm with *Spitzer*. They did not detect any outflow from this source using CO(3–2) APEX observations (beam of ∼3000 au). NH_3 observations by Väisälä et al. (2014) with a resolution of ∼1300 au report only tentative evidence of an outflow. Recently, Busch et al. (2020) showed CO(3–2) ALMA observations with a resolution of ∼0.5 arcsec (100 au) that confirm Cha-MMS1 as the driving source of a small outflow, with a project lobe length of about 2400 au. They determined deprojected outflow speeds of tens of km s^{-1}, in disagreement with model predictions for outflows driven by FHSCs. In Section 4.5.2, we discuss complementary Archive ALMA cycle 2 observations of CO(2–1) and CS(5–4) towards the outflow (Fig. 13).

Cha-MMS1 is one of nine young low-mass stars within a radius of ∼0.2 pc. The outflow from the nearby Class I source IRS4 (14 000 au to the northeast of Cha-MMS1) appears to be interacting with Cha-MMS1 envelope (Belloche et al. 2006; Hiramatsu et al. 2007; Ladd et al. 2011). Our ALMA maps also show evidence of this interaction. Fig. 12 shows the single-dish CO(3–2) blue-shifted (0–3 km s^{-1}) outflow emission arising from IRS 4 (from Hiramatsu et al. 2007) overlaid on our ALMA (12m, 7m, and TP combined) molecular lines maps. The moment maps show that the IRS4 outflow appears to change direction at the position of high-intensity emission of our high-density tracer (NH_2D, see Fig. 12). In addition, the N_2H^+(1–0), $H^{13}CO^+$(1–0), and $CH_3OH(2_{0,2}–1_{0,1})$ show blue-shifted velocities and/or broad linewidths at the south-western edge of the IRS4 outflow. In the HCO^+(1–0) and HCN(1–0) maps, we also see enhanced emission in the regions where the south-western edge of

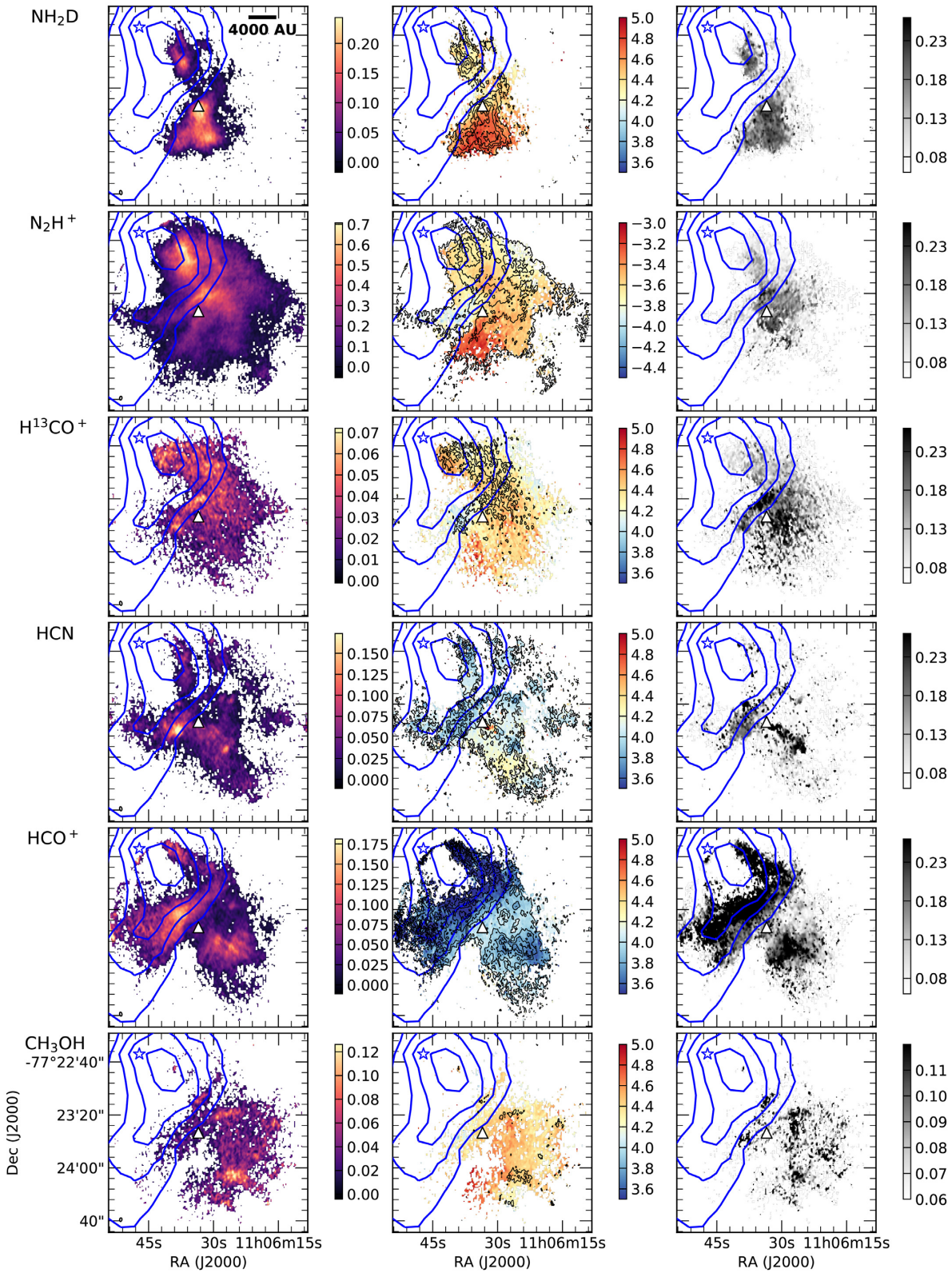

Figure 12. Cha-MMS1, same as Fig. 6 but with the addition of the ALMA Total Power Array observations. Blue contours show the CO(3–2) integrated intensity for the velocity range between 0.4 and 3 km s^{-1}, reproduced from Ladd et al. (2011) and Hiramatsu et al. (2007). The position of IRS4 (upper left corner) is marked with a star.

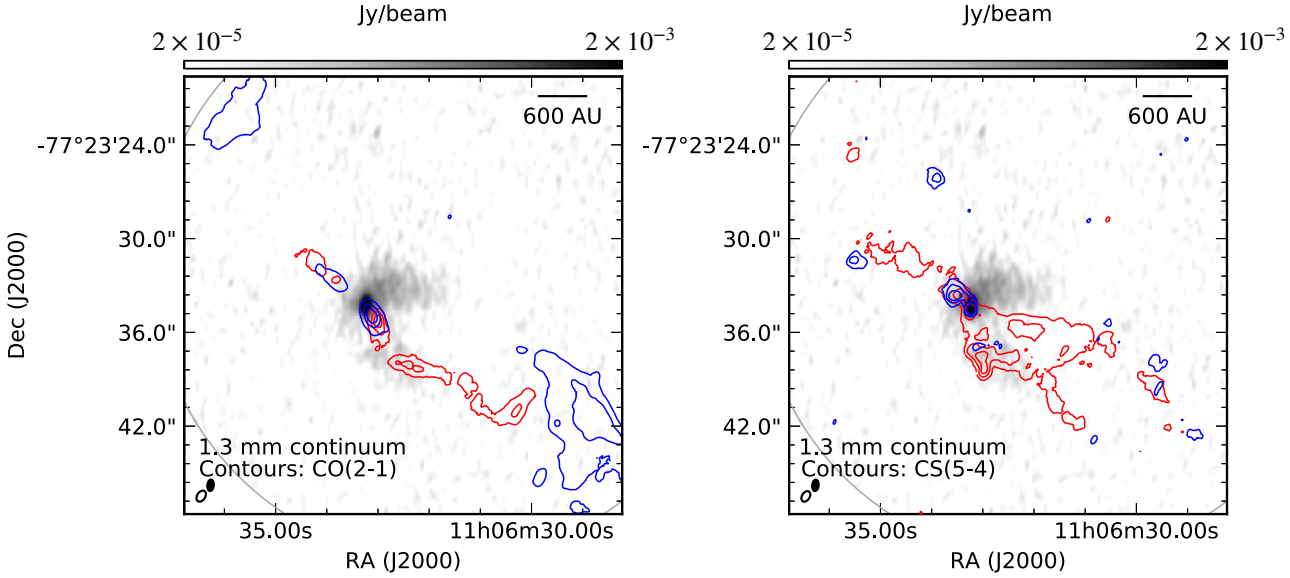

Figure 13. ALMA observations showing the outflow driven by Cha-MMS1. Both panels show the 1.3 mm continuum emission in grey-scale. *Left:* Contours show CO(2–1) blue-shifted (1.9–3.6 km s^{-1}) and red-shifted (5.8–14.7 km s^{-1}) integrated intensity (the systemic velocity of this source is 4.5 km s^{-1}). Contours start at 10 per cent of the maximum and increase in steps of 30 per cent. The maxima of the blue-shifted and red-shifted emission are 0.2 and 0.1 Jy beam^{-1} km s^{-1}, respectively. *Right:* Contours show CS(5-4) blue-shifted (4.0–4.2 km s^{-1}) and red-shifted (4.6–5.5 km s^{-1}) integrated intensity. The maxima of the blue-shifted and red-shifted emission are 0.01 and 0.04 Jy beam^{-1} km s^{-1}, respectively. The beam sizes are indicated in the bottom left corner with a filled and open ellipse for the continuum and molecular line, respectively. The solid grey line marks the 20 per cent level of the primary beam.

the IRS 4 outflow overlaps with the Cha-MMS1 core. This is similar to what we see in the L1448 region (Fig. 2), and it is likely related to a shock-induced abundance enhancement of these molecules. Our observations therefore provide further support to the scenario that the IRS4 outflow is interacting with (and it is deflected by) the Cha-MMS1 dense envelope material.

In our $NH_2D(1_{1,1}–1_{0,1})$ observations, the peak emission is offset by approximately 850 au south-west from Cha-MMS1 (Fig. 6). It is not clear if this is due to the source's evolution or because the outflow from IRS 4 is pushing the dense gas towards the south-west. The steep gradient in intensity of $NH_2D(1_{1,1}–1_{0,1})$ at the border facing the IRS 4 outflow, as well as the velocity gradient (in the same direction) suggests that the $NH_2D(1_{1,1}–1_{0,1})$ could be offset due to the impact from the outflow. Similarly, the N_2H^+(1–0), although present at the position of the source, is weak in comparison with other positions in the region, and does not peak at the continuum peak position, consistent with the source being firmly in the Class 0/I phase. However, the $H^{13}CO^+$(1–0), HCN(1–0), HCO^+(1–0), and $CH_3OH(2_{0,2}–1_{0,1})$ are all weak and/or not present towards the compact continuum source (Figs 6 and A5), as expected for sources in an extremely young evolutionary state, FHSC or very young Class 0 protostar.

4.5.1 *Infall and rotation*

Fig. 9 shows the position–velocity diagrams of the $NH_2D(1_{1,1}–1_{0,1})$ and N_2H^+(1–0) along a cut perpendicular and parallel to the outflow of this source ($PA_{out} = 46°$, Fig. 13). Along the outflow direction, both lines show a velocity gradient, possibly related to the interaction with the outflow powered by IRS4. Perpendicular to the outflow, both lines show almost no velocity gradient, which can be interpreted as small or no rotational motions at these scales (500 au to few 1000 au). The N_2H^+(1–0) shows a double-peak profile in both cuts. These velocity components correspond to the blue-shifted structure to the north-east and red-shifted structure to the south-west of the source seen in the moment maps (Fig. 6). We use our kinematic model (Appendix C) to provide an upper limit to the mass of the central object. We obtain values of $0.02^{+0.02}_{-0.02}$ $M_\odot$ and $0.04^{+0.02}_{-0.02}$ $M_\odot$ using $NH_2D(1_{1,1}–1_{0,1})$ and N_2H^+(1–0), respectively. The estimate of the disc radius from our best models range from 0 to 300 au. Unlike the results for Perbolo 58 and L1451-mm that required a disc of at least 100 au in radius. Similar to L1451-mm, the estimated upper limit to the mass is small, compared with observations of Class 0 and 0/I protostars at comparable scales and using similar methods (Yen et al. 2015).

4.5.2 *Outflow*

ALMA archive observations of CO (2–1) with a resolution of ∼0.5 arcsec (100 au) show the outflow driven by Cha-MMS1. Fig. 13 exhibit blue- and red-shifted outflow velocities between about 1–3 km s^{-1} and between about 1 and 10 km s^{-1}, respectively. In Busch et al. (2020), they detect CO (3–2) blue-shifted outflow velocities of up to about 11 km s^{-1}, and red-shifted outflow velocities of up to 17 km s^{-1}, thus tracing higher velocity gas than the CO (2–1) observations (which could due to the lower sensitivity, by a factor of 2, in observations of the lower transition). The CO outflow shows mostly a jet-like morphology with a PA of ∼46°. The blue-shifted and red-shifted emission overlap on both sides of the continuum emission, indicating an orientation close to the plane of sky. Busch et al. (2020) derive an angle of less than 20 deg between the outflow axis and the plane of sky. The maximum projected extension as measured in the south-west lobe is about 2700 au. The estimate of the projected dynamical time is $\lesssim$10 000 yr, similar to other FHSC candidates (Dunham et al. 2011).

Fig. 13 also shows the integrated red-shifted and blue-shifted emission from CS(5–4). The velocity ranges of the integrated intensity are 4.0–4.2 and 4.6–5.5 km s^{-1}, and the systemic velocity of the source is 4.5 km s^{-1}. Similar to the CO outflow, the CS outflow show blue- and red-shifted emission in both lobes. However,

the morphology of the south-west CS lobe shows a clear cone-shaped structure, unlike the jet-like structure traced by the CO. Our Cycle 1 ALMA HCN(1–0) observations also evidence of outflow emission. This can be seen in Figs 6 and 11 that show red-shifted emission with velocities about 1 km s^{-1} away from the systemic velocity, and consistent with the direction of the CO and CS outflow. A detailed characterization of the morphology of the CO outflow is beyond the scope of this paper, and will be addressed in a follow-up paper.

Summarizing, our ALMA maps and the small CO outflow are consistent with a very young evolutionary state for this candidate. Although we cannot securely discriminate between an FHSC or a young Class 0 protostar with the current data, the CO outflow morphology and a maximum projected outflow velocities of about 10 km s^{-1} suggest Cha-MMS1 already formed a protostar as suggested in previous independent studies (Young et al. 2018; Busch et al. 2020).

5 DISCUSSION

In Fig. 14, we attempt to summarize and compare the properties of former and current FHSC candidates presented in this work and the literature. In the top panel, we show normalized SEDs for the sources proposed as FHSC candidates and compared them to young Class 0 protostars ($T_{\rm bol} \lesssim 50$ K) from the literature. From this comparison, it is clear that the sources proposed as FHSC candidates appear generally younger than the average SED for a young Class 0 protostar, as the SED of FHSC candidates peaks at longer wavelengths and all show lower normalized flux at 70 μm, compared to the average Class 0 SEDs. Nevertheless, some FHSC candidates do look more evolved (Per-bolo 58, Cha-MMS1, B1b-S, and Aqu-MM1) than others, as their 70 μm fluxes are close to the lower end of the range of the young Class 0 sources observed in Fig. 14. These FHSC candidates with more evolved SEDs (except Aqu-MM1[1]) show evidence in support of a young Class 0 stage, when viewed with interferometric observations. Most of the evidence comes from the detection of high-velocity components in their outflow (B1b-S, Hirano 2019; Cha-MMS1, Busch et al. 2020) and/or from the distribution of molecular line emission at the inner envelope or disc scales (Per-bolo 58, Section 4.3 in this work; B1b-S Marcelino et al. 2018).

The rest of the FHSC candidates shows normalized SEDs with significantly less flux at short wavelengths from the peak (compared to average Class 0 SEDs), consistent with them being at a younger evolutionary state. Among these, there is Per-bolo 45 for which our observations indicate it is likely pre-stellar (Section 4.2, see also Stephens et al. 2019). Included in this group is also B1b-N that was recently confirmed as a young Class 0 protostar owing to the newly detected high-velocity outflow component (projected maximum velocity of 9 km s^{-1}) traced by methanol (Hirano 2019). The two remaining sources, K242 and L1451-mm show the least evolved SEDs. The former was proposed as a FHSC by Young et al. (2018) based on modelling of the SED. However, there are no more constraints of the evolutionary state of this source as it currently lacks interferometric observations. As for L1451-mm, in Section 4, we analysed this source and concluded that it was consistent with either an extremely young Class 0 protostar or a FHSC. The bottom panels in Fig. 14 show a comparison of L1451-mm properties observed with interferometric observations with that of other FHSC candidates with outflow detection. In particular, the bottom left-hand panel shows the CO outflow properties (maximum velocity, maximum lobe length) and the bottom right-hand panel compares the distance between the dust emission peak and the emission peak of a cold/high-density gas tracer (such as NH_2D and N_2D^+). In both panels, the younger the source, the closer it should lie to the lower left corner. From these plots, the most promising FHSC candidate in our sample, L1451 mm, appears as the youngest source. Although more evolved than L1451-mm (according to its position in the bottom panels of Fig. 14), the recently identified source in Taurus (MC35-mm, Fujishiro et al. 2020) may still be considered an FHSC candidate. Two other FHSC candidates can be found in the literature but are not shown in Fig. 14 due to their lack of confirmed outflow emission. These are SM1N and Oph A-N6, both located in Ophiuchus. Although typically considered as pre-stellar in nature, recent ALMA high-resolution observations revealed that they are not resolved-out and instead remain detected and showing concentrated continuum emission at 100 au scales (Friesen et al. 2018). The observations in Friesen et al. (2018) show no clear evidence in the CO (2–1) emission of outflows towards SM1N and Oph A-N6. Red-shifted emission on one side of Oph A-N6 extending up to ∼1400 au is suggestive, but further observations perhaps with a different tracer are needed to confirm this, since as pointed out in Friesen et al. (2018), any outflow from this source will be difficult to detect due to contamination from VLA 16293's outflow. Both sources also show significant emission of deuterated species (Bourke et al. 2012; Friesen et al. 2014), peaking at similar distances from the continuum as L1451-mm (see Table D1).

For these four remaining FHSC candidates (L1451-mm, MC35-mm, SM1N, and Oph A-N6) that have been observed at intermediate scales (few 100 au to few 1000 au) a final confirmation of their true evolutionary state requires higher resolution observations. For L1451-mm, the compact outflow needs to be resolved to investigate its morphology and kinematics, as a higher velocity component (an indication of protostellar nature) could be revealed by observations with a beam smaller than 100 au, similar to the case of B1b-N (Hirano 2019). An additional goal of high-resolution observations for L1451-mm and the remaining youngest candidates should be to investigate the temperature and density profiles of the envelope at scales from few au to 100 au. This is because simulations show that the temperature remains lower than ∼30 K even at several tens of au up to 100 au from the centre (Bate et al. 2014; Tomida et al. 2015; Hincelin et al. 2016; Young et al. 2019) during the FHSC stage. On the other hand, Class 0 sources show temperatures of 20–30 K or higher at scales of several 100 au (sufficient for thermal evaporation of CO) that results in the inner envelope and disc being easily detected using $C^{18}O$ observations (Yen et al. 2015, 2017; Stephens et al. 2018). This holds even in very low luminosity objects, for which the unexpected large extent of $C^{18}O$ is interpreted as evidence of a previous burst of accretion (Frimann et al. 2017; Hsieh et al. 2018). As for the density profile, simulations of the FHSC stage show a flat inner region, corresponding to the FHSC structure and extending up to ∼10 au (Tomida et al. 2013; Bate et al. 2014). For a protostar, on the other hand, the density profile should increase towards the central ∼1 au region (Young et al. 2019). Observations of the continuum emission with a resolution better than a few tens of au are likely required to model the emission and provide a density and temperature profile that can probe the relevant scales. Additional line observations with a similar resolution can also help to further distinguish between the different models. We note that, as pointed out in Young et al. (2019), distinguishing a dense core with only an FHSC and one that has recently formed a protostar but in which the FHSC structure is still present is likely not possible, even with high-resolution observations.

[1]To date, there are no interferometric observations probing the existence of an outflow or the emission properties of dense gas tracers.

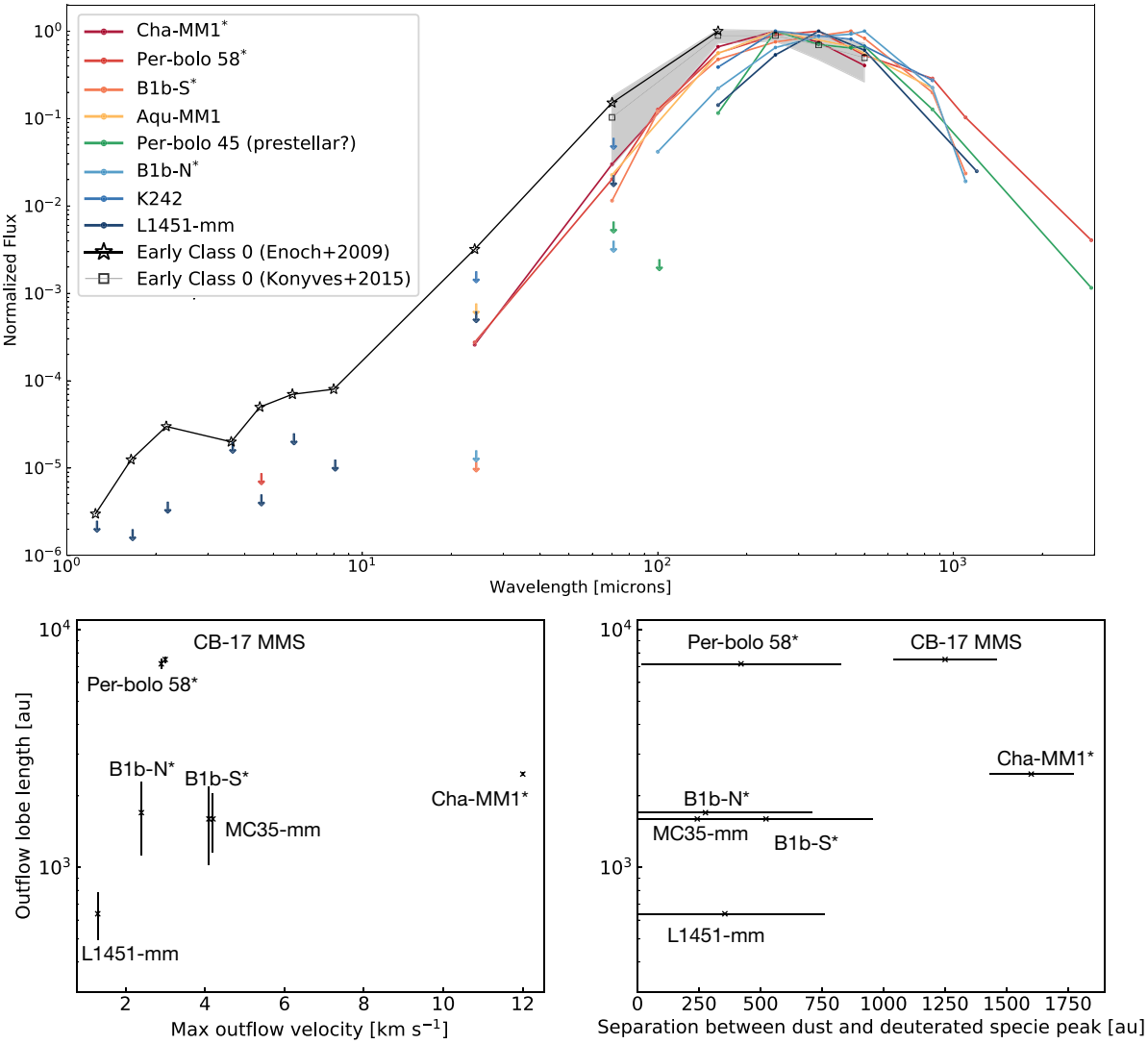

Figure 14. Comparison of current and former FHSC candidates in this work and the literature. Former FHSC candidates that have evidence for being young Class 0 sources are marked with ∗ next to their names. *Top:* Normalized spectral energy distributions. SEDs are normalized such that their peak correspond to a value of 1. Normalized SEDs for proposed FHSC candidates are shown in different colours. The average SED of early Class 0 sources ($T_{\rm bol} \lesssim 50$ K) from Enoch et al. (2009) (black line with stars symbols) and the average SED of early Class 0 ($T_{\rm bol} \lesssim 50$ K) from Maury et al. (2011) and Könyves et al. (2015) (grey line with square symbols) are also shown for comparison. The dispersion around the average for the later is shown as a grey shaded area. Bottom left: CO molecular outflow lobe length versus their maximum projected velocity. Error bars in the outflow lobe length correspond to half the beam minor axis of the observations of the respective sources. For Per-bolo 58, the outflow lobe length is an upper limit, since the outflow is detected out to the edge of the primary beam (Dunham et al. 2011). Bottom right: CO molecular outflow lobe length versus the distance between the peak of the integrated emission of a deuterated species (typically NH_2D or N_2D^+). The error bars for the outflow lobe length are the same as in the left-hand panel and were omitted for clarity. The error bars for the distance between the peak of the integrated emission of a deuterated species correspond to half the beam minor axis of the observations of the respective sources. Values in these figures and their references are listed in Table D1.

Given the optically thick nature of the FHSC core, it is difficult to probe the physical properties within the FHSC structure. Despite this, finding a source with density and temperature profiles as well as with outflow properties consistent with the theoretical predictions will provide convincing evidence in support of a bona fide FHSC.

Under the assumption of constant star formation rate, Pineda et al. (2011) estimated the number of FHSC expected in the Perseus molecular cloud, as a fraction (proportional to the lifetime of a FHSC) of the current Class 0 sources. They concluded that the number of candidates (Per-bolo 58, L1451-mm, Per-bolo 45, and L1448 IRS2E) was inconsistent with the theoretical predictions. We can reassess this analysis in light of our results. Using a lifetime of the Class 0 stage of 0.2 Myr (Dunham et al. 2014), then in the scenario in which the FHSC lifetime is close to 10^4 yr, we would require at least 20 Class 0 sources to expect one FHSC. This number increases up to 200 if the lifetime is 10^3 yr. Since there are about 38 Class 0 sources in Perseus (Dunham et al. 2015), one or two FHSCs are expected if the lifetime is several 10^3 yr or more. This is consistent with our results that indicate there is only one FHSC candidate in Perseus (L1451-mm). Given the low number of embedded protostars in the Chamaeleon I molecular cloud (<10, Dunham et al. 2016), the confirmation of Cha-MMS1 as the only Class 0 protostar (and not a FHSC) in this cloud is also in agreement with the theoretical expectations. Finally, we note that most of the proposed FHSC candidates have been found

serendipitously. Unbiased interferometric surveys towards a large number of starless cores (e.g. Dunham et al. 2016; Kirk et al. 2017 and more recently Tokuda et al. 2020) are an efficient way to find sources on the verge of star formation, such an FHSC. Thus, future similar surveys towards regions with a larger number of starless and young protostellar sources are needed to improve the chances of observing a bona fide FHSC.

6 SUMMARY AND CONCLUSION

We studied the emission properties and kinematics at envelope scales of five FHSC candidates; four located in the Perseus molecular cloud and one located in the Chamaeleon molecular cloud. We used 3 mm molecular lines and continuum ALMA observations with a resolution of 3.5–4 arcsec (∼700–1160 au). Our results can be summarized as follows:

(i) Two out of the five candidates remain consistent with a very young evolutionary state: L1451-mm and Cha-MMS1. The isolated source L1451 mm shows envelope and outflow properties that are extremely rare among typical Class 0 sources and even other FHSC candidates, which suggest that it is one of the youngest (if not the youngest) known low-mass protostellar source and thus a promising FHSC candidate. Cha-MMS1's envelope does not show definitive evidence to rule it out as an FHSC candidate (or confirm it as a Class 0 protostar). Yet, the collimated morphology of its CO molecular outflow and high-deprojected velocities suggests Cha-MMS1 is already in the protostellar phase.

(ii) Among the remaining three sources in our sample (Per-bolo 58, Per-bolo 45, and L1448 IRS2E), we classify Per-bolo 58 as a young Class 0 protostar on the basis of the properties of its envelope and outflow, which are inconsistent with those expected for FHSC. Per-bolo 45 continuum emission is elongated and almost resolved out in the interferometer data. This, along with a lack of conclusive evidence for an embedded outflow, firmly favours a pre-stellar (pre-FSHC) stage for this candidate. In the case of L1448 IRS2E, our observations support that there is no core (pre or protostellar) at this location (see below).

(iii) We did not detect any 3 mm continuum or evidence of dense gas (traced by N_2H^+ and NH_2D) towards the FHSC candidate L1448 IRS2E. Our maps show evidence that the gas in this location is impacted by the nearby outflow from the Class 0 protostellar system L1448 IRS2. Given the morphology of the carved gas as well as the velocities of the proposed L1448 IRS2E's CO outflow (and other outflow tracers), a more natural explanation for the non-detection of the continuum is that the red-shifted emission interpreted as an outflow from L1448 IRS2E by Chen et al. (2010) is emission from the nearby outflow that has been deflected by the dense gas present at the location where the FHSC candidate was thought to be.

Our observations show that not all sources proposed as FHSC candidates, based on their SED and/or the detection of dust and outflow in interferometric observations, pass the test of truly being in an extremely young evolutionary state (FHSC or extremely young protostar). Thus, observations of the inner and outer envelopes of FHSC candidates are a useful and efficient tool to identify the most promising candidates. The two youngest sources identified in this work (L1451-mm and Cha-MMS1) are rare and unique laboratories for investigating the earliest stages of star formation. Future observations at envelope-disc and disc scales down to 10 au resolution towards the most promising candidate in this work (L1451-mm) as well as those in the literature will serve to constrain models of core collapse and disc formation, as well as to further discriminate their true nature.

ACKNOWLEDGEMENTS

MJM and HGA acknowledge support from the National Science Foundation award AST-1714710. DM acknowledges support from CONICYT project Basal AFB-170002. MJM and JEP are grateful for support from the Max Planck Society.

We thank Ned Ladd for providing us with the CO(3–2) single dish data for Cha-MMS1. This paper makes use of the following ALMA data: ADS/JAO.ALMA#2012.1.00394.S and ADS/JAO.ALMA#2013.1.01113.S. ALMA is a partnership of ESO (representing its member states), NSF (USA) and NINS (Japan), together with NRC (Canada), MOST and ASIAA (Taiwan), and KASI (Republic of Korea), in cooperation with the Republic of Chile. The Joint ALMA Observatory is operated by ESO, AUI/NRAO, and NAOJ.

DATA AVAILABILITY

The raw data is available on the ALMA archive ADS/JAO.ALMA#2012.1.00394.S, ADS/JAO.ALMA#2013.1.01113.S. The calibrated and imaged data underlying this article will be shared on reasonable request to the corresponding author.

REFERENCES

Andre P., Ward-Thompson D., Barsony M., 2000, in Mannings V., Boss A. P., Russell S. S., eds, Protostars and Planets IV, The University of Arizona Pres, p. 59
Balog Z. et al., 2014, Exp. Astron., 37, 129
Bate M. R., Tricco T. S., Price D. J., 2014, MNRAS, 437, 77
Belloche A., Parise B., van der Tak F. F. S., Schilke P., Leurini S., Güsten R., Nyman L. Å., 2006, A&A, 454, L51
Bendo G. J. et al., 2013, MNRAS, 433, 3062
Bergin E. A., Tafalla M., 2007, ARA&A, 45, 339
Bourke T. L., Myers P. C., Caselli P., Di Francesco J., Belloche A., Plume R., Wilner D. J., 2012, ApJ, 745, 117
Bracco A. et al., 2017, A&A, 604, A52
Busch L. A., Belloche A., Cabrit S., Hennebelle P., Commerçon B., 2020, A&A, 633, A126
Caselli P., Walmsley C. M., Zucconi A., Tafalla M., Dore L., Myers P. C., 2002, ApJ, 565, 344
Chen X., Arce H. G., Zhang Q., Bourke T. L., Launhardt R., Schmalzl M., Henning T., 2010, ApJ, 715, 1344
Chen X., Arce H. G., Dunham M. M., Zhang Q., Bourke T. L., Launhardt R., Schmalzl M., Henning T., 2012, ApJ, 751, 89
Chen M. C.-Y. et al., 2016, ApJ, 826, 95
Commerçon B., Launhardt R., Dullemond C., Henning T., 2012, A&A, 545, A98
Daniel F. et al., 2016, A&A, 586, L4
Dunham M. M., et al., 2014, in Beuther H., Klessen R. S., Dullemond C. P. , Henning T., eds, Protostars and Planets VI, University of Arizona Press, Tucson, p. 195
Dunham M. M. et al., 2015, ApJS, 220, 11
Dunham M. M. et al., 2016, ApJ, 823, 160
Dunham M. M., Chen X., Arce H. G., Bourke T. L., Schnee S., Enoch M. L., 2011, ApJ, 742, 1
Dzib S. A., Loinard L., Ortiz-León G. N., Rodríguez L. F., Galli P. A. B., 2018, ApJ, 867, 151
Enoch M. L., Evans N. J., Sargent A. I., Glenn J., Rosolowsky E., Myers P., 2008, ApJ, 684, 1240
Enoch M. L., Evans Neal J. I., Sargent A. I., Glenn J., 2009, ApJ, 692, 973
Enoch M. L., Lee J.-E., Harvey P., Dunham M. M., Schnee S., 2010, ApJ, 722, L33
Friesen R. K., Di Francesco J., Bourke T. L., Caselli P., Jørgensen J. K., Pineda J. E., Wong M., 2014, ApJ, 797, 27

Friesen R. K., Pon A., Bourke T. L., Caselli P., Di Francesco J., Jørgensen J. K., Pineda J. E., 2018, ApJ, 869, 158
Frimann S. et al., 2017, A&A, 602, A120
Fuente A. et al., 2017, A&A, 606, L3
Fujishiro K. et al., 2020, ApJ, 899, L10
Gerin M., Pety J., Fuente A., Cernicharo J., Commerçon B., Marcelino N., 2015, A&A, 577, L2
Griffin M. J. et al., 2013, MNRAS, 434, 992
Guzmán A. E., Sanhueza P., Contreras Y., Smith H. A., Jackson J. M., Hoq S., Rathborne J. M., 2015, ApJ, 815, 130
Hatchell J., Fuller G. A., Richer J. S., Harries T. J., Ladd E. F., 2007, A&A, 468, 1009
Hincelin U., Wakelam V., Commerçon B., Hersant F., Guilloteau S., 2013, ApJ, 775, 44
Hincelin U., Commerçon B., Wakelam V., Hersant F., Guilloteau S., Herbst E., 2016, ApJ, 822, 12
Hiramatsu M., Hayakawa T., Tatematsu K., Kamegai K., Onishi T., Mizuno A., Yamaguchi N., Hasegawa T., 2007, ApJ, 664, 964
Hirano N., 2019, ALMA2019: Science Results and Cross-Facility Synergies. p. 90
Hirano N., Liu F.-c., 2014, ApJ, 789, 50
Hogerheijde M. R., 2001, ApJ, 553, 618
Hsieh T.-H., Murillo N. M., Belloche A., Hirano N., Walsh C., van Dishoeck E. F., Lai S.-P., 2018, ApJ, 854, 15
Jiménez-Serra I., Caselli P., Tan J. C., Hernand ez A. K., Fontani F., Butler M. J., van Loo S., 2010, MNRAS, 406, 187
Jørgensen J. K., Schöier F. L., van Dishoeck E. F., 2005, A&A, 435, 177
Kirk H. et al., 2017, ApJ, 838, 114
Kirk H., Johnstone D., Di Francesco J., 2006, ApJ, 646, 1009
Könyves V. et al., 2015, A&A, 584, A91
Ladd E. F., Wong T., Bourke T. L., Thompson K. L., 2011, ApJ, 743, 108
Larson R. B., 1969, MNRAS, 145, 271
Lee J.-E., Bergin E. A., Evans N. J., II, 2004, ApJ, 617, 360
Machida M. N., 2014, ApJ, 796, L17
Machida M. N., Inutsuka S.-I., Matsumoto T., 2008, ApJ, 676, 1088
Machida M. N., Inutsuka S.-I., Matsumoto T., 2014, MNRAS, 438, 2278
Marcelino N. et al., 2018, A&A, 620, A80
Masunaga H., Miyama S. M., Inutsuka S.-I., 1998, ApJ, 495, 346
Matsumoto T., Hanawa T., 2011, ApJ, 728, 47
Maureira M. J., Arce H. G., Dunham M. M., Pineda J. E., Fernández-López M., Chen X., Mardones D., 2017a, ApJ, 838, 60
Maureira M. J., Arce H. G., Offner S. S. R., Dunham M. M., Pineda J. E., Fernández-López M., Chen X., Mardones D., 2017b, ApJ, 849, 89
Maury A. J. et al., 2019, A&A, 621, A76
Maury A. J., André P., Men'shchikov A., Könyves V., Bontemps S., 2011, A&A, 535, A77
Ohashi N. et al., 2014, ApJ, 796, 131
Ortiz-León G. N. et al., 2018, ApJ, 865, 73
Ossenkopf V., Henning T., 1994, A&A, 291, 943
Oya Y. et al., 2014, ApJ, 795, 152
Pezzuto S. et al., 2012, A&A, 547, A54
Pineda J. E. et al., 2011, ApJ, 743, 201
Pineda J. E., Zhao B., Schmiedeke A., Segura-Cox D. M., Caselli P., Myers P. C., Tobin J. J., Dunham M., 2019, ApJ, 882, 103
Plunkett A. L., Arce H. G., Corder S. A., Mardones D., Sargent A. I., Schnee S. L., 2013, ApJ, 774, 22
Price D. J., Tricco T. S., Bate M. R., 2012, MNRAS, 423, L45
Roccatagliata V., Sacco G. G., Franciosini E., Randich S., 2018, A&A, 617, L4
Sadavoy S. I. et al., 2010, ApJ, 710, 1247
Sadavoy S. I. et al., 2012, A&A, 540, A10
Saigo K., Tomisaka K., 2006, ApJ, 645, 381
Schnee S., Di Francesco J., Enoch M., Friesen R., Johnstone D., Sadavoy S., 2012, ApJ, 745, 18
Segura-Cox D. M. et al., 2018, ApJ, 866, 161
Stephens I. W. et al., 2018, ApJS, 237, 22
Stephens I. W. et al., 2019, ApJ, 245, 21
Suutarinen A. N., Kristensen L. E., Mottram J. C., Fraser H. J., van Dishoeck E. F., 2014, MNRAS, 440, 1844
Tokuda K. et al., 2020, ApJ, 899, 10
Tomida K., Tomisaka K., Matsumoto T., Hori Y., Okuzumi S., Machida M. N., Saigo K., 2013, ApJ, 763, 6
Tomida K., Okuzumi S., Machida M. N., 2015, ApJ, 801, 117
Tsitali A. E., Belloche A., Commerçon B., Menten K. M., 2013, A&A, 557, A98
Tsukamoto Y., Okuzumi S., Iwasaki K., Machida M. N., Inutsuka S., 2018, ApJ, 868, 22
Ulrich R. K., 1976, ApJ, 210, 377
Väisälä M. S., Harju J., Mantere M. J., Miettinen O., Sault R. S., Walmsley C. M., Whiteoak J. B., 2014, A&A, 564, A99
Yen H.-W., Takakuwa S., Ohashi N., Ho P. T. P., 2013, ApJ, 772, 22
Yen H.-W., Koch P. M., Takakuwa S., Ho P. T. P., Ohashi N., Tang Y.-W., 2015, ApJ, 799, 193
Yen H.-W., Koch P. M., Takakuwa S., Krasnopolsky R., Ohashi N., Aso Y., 2017, ApJ, 834, 178
Young A. K., Bate M. R., Mowat C. F., Hatchell J., Harries T. J., 2018, MNRAS, 474, 800
Young A. K., Bate M. R., Harries T. J., Acreman D. M., 2019, MNRAS, 487, 2853
Zucker C., Schlafly E. F., Speagle J. S., Green G. M., Portillo S. K. N., Finkbeiner D. P., Goodman A. A., 2018, ApJ, 869, 83

APPENDIX A: SPECTRA AT THE POSITION OF THE SOURCES

Figs A1–A5 show the spectra of all the species we observe towards the position of the FHSC candidates in our study.

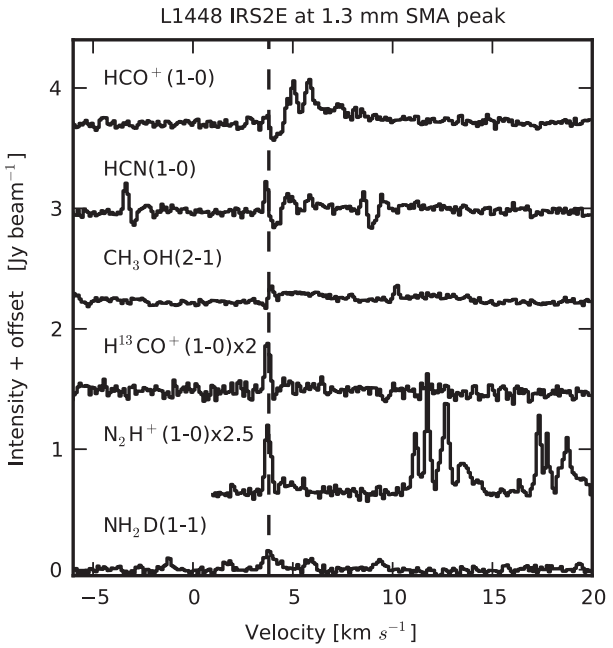

Figure A1. L1448IRS2E molecular line spectra at the 1.3 mm SMA continuum peak in Chen et al. (2010). The vertical lines corresponds to 3.8 km s^{-1}, the presumed systemic velocity of the envelope at the location of candidate. The spectra are averaged over a beam.

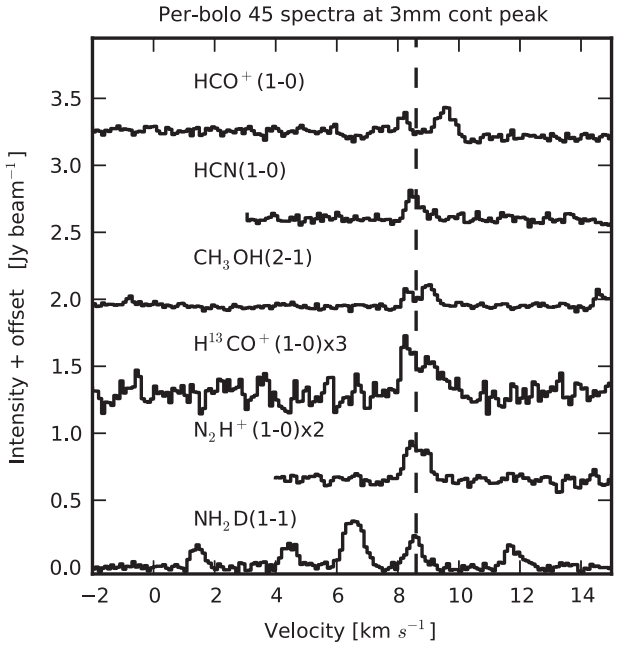

Figure A2. Per-bolo 45 molecular line spectra averaged over a beam at the position of the 3 mm continuum peak. The vertical line corresponds to 8.6 km s^{-1}, the presumed systemic velocity of the envelope at the location of candidate. The N_2H^+(1–0) spectrum is shifted to show the isolated hyperfine component. The $NH_2D(1_{1,1}–1_{0,1})$ and HCN(1–0) spectra are also shifted to show a satellite group of hyperfines lines and the weaker hyperfine lines, respectively.

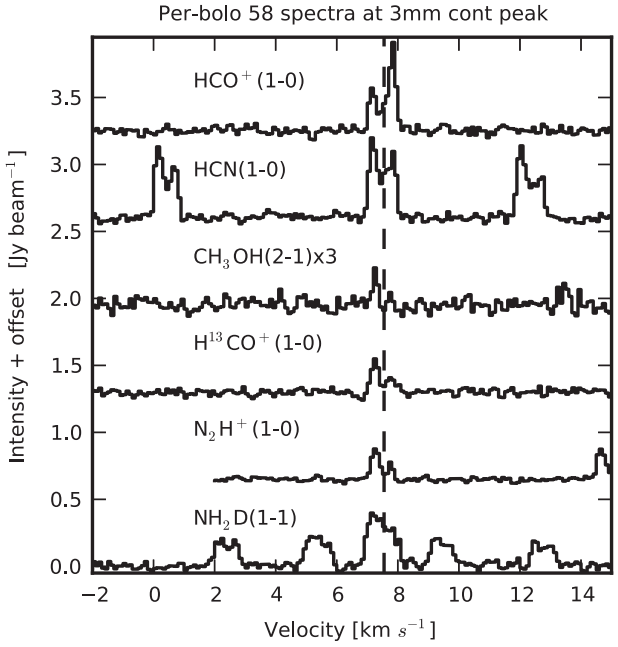

Figure A3. Per-bolo 58 molecular line spectra averaged over a beam at the position of the 3 mm continuum peak. The vertical line corresponds to $v = 7.55$ km s^{-1}, the presumed systemic velocity of the envelope at the location of candidate. The N_2H^+(1–0) spectrum is shifted to show the isolated hyperfine component.

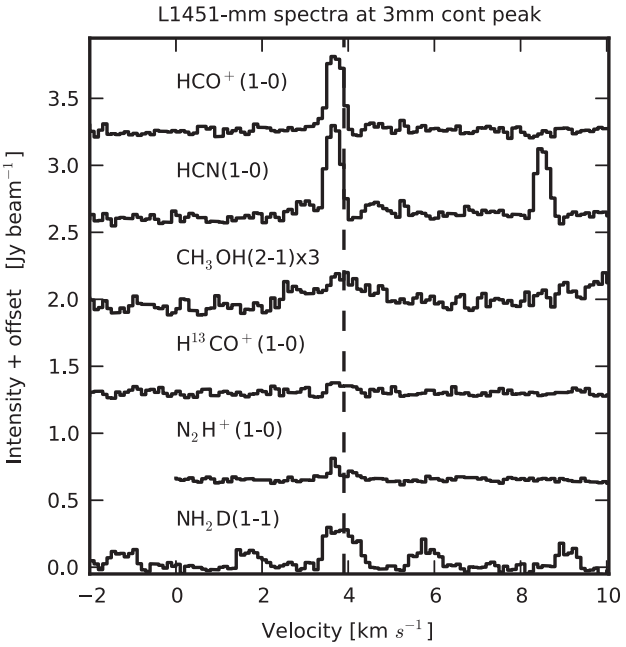

Figure A4. L1451-mm molecular line spectra averaged over a beam at the position of the 3 mm continuum peak. The vertical line corresponds to $v = 3.9$ km s^{-1}, the presumed systemic velocity of the envelope at the location of candidate. The N_2H^+(1–0) spectrum is shifted to show the isolated hyperfine component.

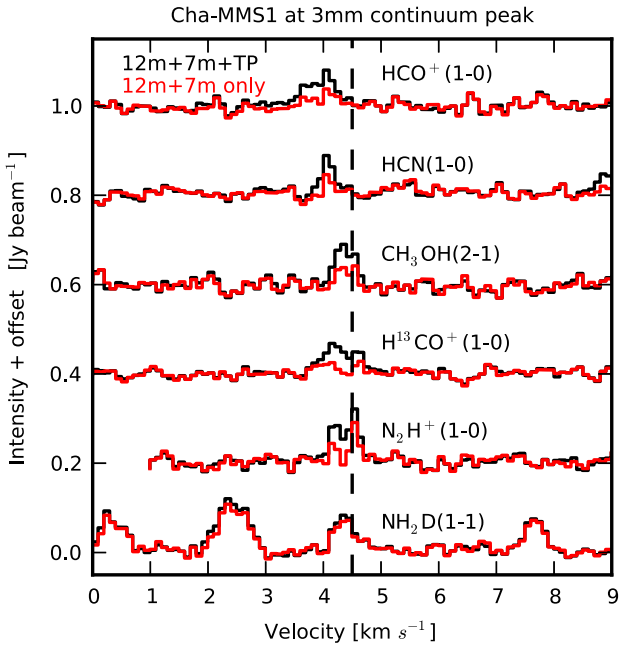

Figure A5. Cha-MMS1 molecular line spectra averaged over a beam at the position of the 3 mm continuum peak with (black) and without (red line) the TP observations. The vertical line corresponds to $v = 4.5$ km s^{-1}, the presumed systemic velocity of the envelope at the location of candidate. The N_2H^+(1–0) spectrum is shifted to show the isolated hyperfine component. The $NH_2D(1_{1,1}–1_{0,1})$ spectrum is also shifted to show a satellite group of hyperfine lines.

APPENDIX B: POSITION–VELOCITY MAP USING $NH_2D(1_{1,1}–1_{0,1})$ SATELLITES

For Per-bolo 58 and Cha-MMS1 the position–velocity maps in Fig. 9 were constructed using the most blue-shifted satellite. This satellite has three hyperfine components (Daniel et al. 2016) separated by less than our channel width (0.1 km s^{-1}). The middle hyperfine at 85.927724 GHz is the brightest and we use this frequency for the rest frequency when constructing the map.

For L1451 mm, the most blue-shifted satellite by itself was too faint to use it for kinematics analysis. Thus, we constructed a position velocity map by averaging the position–velocity map of the four $NH_2D(1_{1,1}–1_{0,1})$ satellites. Each satellite has one or more hyperfine lines with an intensity of at least 10 per cent of the brightest hyperfine within the satellite. These neighbouring hyperfine lines are all within 0.2 km s^{-1} of the brightest of the group. Thus, they are not resolved in our observations. The rest-frame frequencies that we used for averaging the position–velocity maps are 85.927724, 85.926864, 85.925688, 85.924748 GHz, corresponding to the main hyperfine in each satellite.

APPENDIX C: INFALL AND ROTATION TOY MODEL

The toy model considers the ballistic motion of particles under the influence of a central mass (Ulrich 1976). The particles start from an spherical surface assumed to be in solid body rotation. The amount of rotation provides the total angular momentum which is conserved along the trajectories and results in a radius at which the infall velocity becomes zero and material cannot continue infalling (i.e. the centrifugal barrier). Before that, the infall velocity reaches its maximum value at a radius two times the centrifugal barrier value. This radius is typically assumed as the radius within which a rotationally supported disc can form (Ulrich 1976). As described in Ulrich (1976) the trajectories and velocities of the particles are fully defined by two parameters: the central mass and the disc (or centrifugal barrier) radius. All the trajectories in this model correspond to parabolas.

As in Maureira et al. (2017a), for a given pair of these parameters we construct a model cube to compare with observations. To produce the cube, given a coordinate position on the sky, we simulate a line of sight that crosses the spherical envelope at that position. The line of sight can have an inclination i such such that if $i = 90^\circ$, the observer is looking through the mid-plane in an edge-on configuration. We calculate the line-of-sight velocity every 10 au steps along a given line of sight. For each of these steps, we calculate a Gaussian centred at that velocity with a linewidth equal to a thermal width at a temperature of 10 K. The amplitude of the Gaussian is set to be proportional to the density at that position assuming a density profile proportional to r^{-2}. The final spectrum along a line of sight is the sum of all the Gaussians along the line of sight. The cube was then convolved to match the beam of the observations and we construct position–velocity maps along the equator and perpendicular to it. To compare the kinematics between the observed and modelled data, for each spatial position along the p–v cut (i.e. for each column in the p–v diagrams), we matched the intensity peak value of the observed spectrum with the modelled one. For all sources, we fix the inclination to $i = 90^\circ$as this provides with an upper limit to the mass (Maureira et al. 2017a). Further details and discussion of the model are included in Maureira et al. (2017a).

For each source we constructed models with masses from 0.02 to 0.22 $M_\odot$ in steps of 0.02 $M_\odot$ and centrifugal barrier radii of 0, 50, 100, and 150 au. Our models do not constrain well the radius of the centrifugal barrier, meaning that the appearance of the p–v diagrams do not change much for different values of this parameter in the range we explored. The upper limit of 150 au was chosen as a limiting extreme case, given that observations show that most protostellar discs are consistent with a radius smaller than 100 au (Segura-Cox et al. 2018; Maury et al. 2019; Pineda et al. 2019). We note, however, that increasing the centrifugal barrier radius results in larger values for the central mass that, in some cases, can match the data. For Per-bolo 58 and L1451-mm, we set the radius of the initial sphere (envelope in our model) to 5000 au, while for Cha-MMS1 we fix it to 2700 au. These values were chosen as they match the extent of the emission observed in the p–v diagrams.

We estimate the best-fitting model and the uncertainty in the derived mass form the model in the following way. For each p–v diagram and model, we calculated $res_{\rm pix}$, in units of σ, corresponding to the residual (i.e. observation minus the model) divided by the rms of the p–v map. The total residual for each p–v diagram and model was then calculated as the maximum $res_{\rm max}$ of the $res_{\rm pix}$ values among all pixels within 15 arcsec of the source position. Then, for each model and molecule we calculated the combined residual $res_{\rm comb}$ corresponding to the geometric mean of the $res_{\rm max}$ values for the model p–v diagrams along the equator (perpendicular to the outflow in the observations) and perpendicular to the equator (parallel to the outflow in the observations). Finally, we report the best-fitting models for each molecule as those that result in the minimum combined residual $res_{\rm comb}$. The errors for the masses were calculated as those models that resulted in a $res_{\rm comb}$ value up to 10 per cent higher than that of the best fit. This percentage usually corresponded to models that had a combined residual value that was approximately 1σ higher than the residual of the best model. We note that calculating residuals as the sum of $res_{\rm pix}$ over all pixels in a p–v diagram results in similar 'best fit' values for the masses obtained using $res_{\rm max}$ (within the provided uncertainties). However, $res_{\rm max}$ provided a more intuitive quantity to assess uncertainties in a uniform way for all sources.

APPENDIX D: PROPERTIES OF FHSC CANDIDATES FROM THIS WORK AND THE LITERATURE

Table D1 lists the outflow and dense gas tracer properties used in Fig. 14 to compare current and former FHSC candidates in this work and in the literature.

D1 Herschel PACS/SPIRE fluxes for Per-bolo 45, Per-bolo 58, and L1451-mm

We performed photometry on the Herschel 160, 250, 350, and 500 μm observations (Pezzuto et al. 2012; Sadavoy et al. 2012) for Per-bolo 45, Per-bolo 58, and L1451-mm, as we could not find these measurements in the literature. Observations were taken using the PACS/SPIRE parallel fast mode, for which the typical photometric uncertainties are given in table 1 from Guzmán et al. (2015). The semimajor axes of the apertures at 250 μm were taken as 25 arcsec × 25 arcsec, 20 arcsec × 25 arcsec, and 25 arcsec × 25 arcsec for Per-bolo 45, Per-bolo 58, and L1451-mm, respectively. The PA for Per-bolo 58 elliptical aperture was 25°. The width for the background annulus was taken as 9 arcsec for all sources. The apertures at 160, 350, and 500 μm were calculated based on the apertures values at 250 μm. If the aperture major and minor axes at 250 μm are A and B, then the apertures axes at the other wavelengths were calculated as $\sqrt{A^2 - \theta_{250}^2 + \theta_{wv}^2}$ and $\sqrt{B^2 - \theta_{250}^2 + \theta_{wv}^2}$ where θ_{wv} is the FWHM

Table D1. Properties of current and former FHSC candidates on the literature.

Source	CO_{out} lobe length[a] (au)	CO_{out} velocity[a] (km s^{-1})	Distance to a deuterated species peak[b] (au)	Comments	References.
L1448 IRS2 E	–	–	8600 ($NH_2D(1_{1,1}–1_{0,1})$)	Ruled-out as a star forming core	1,5, 16
Per-bolo 45	–	–	290[c] ($NH_2D(1_{1,1}–1_{0,1})$)	Weak and extended continuum, likely prestellar	1, 19
Per-bolo 58	>7192	2.9	420[c] ($NH_2D(1_{1,1}–1_{0,1})$, $N_2D^+(3–2)$)	Young Class 0 protostar	1,2,3,4,5
L1451-mm	640	1.3	355[c] ($NH_2D(1_{1,1}–1_{0,1})$, $N_2D^+(3–2)$)	FHSC/young Class 0 protostar	1,5,6
Cha-MMS1	2470	12	1600 ($NH_2D(1_{1,1}–1_{0,1})$)	Young Class 0 protostar	1,4,7,8,9
B1b-N	1700	2.4	276[c] ($N_2D^+(3–2)$)	Young Class 0 protostar	5, 10, 11
B1b-S	1600	4.1	522[c] ($N_2D^+(3–2)$)	Young Class 0 protostar (hot corino)	5,10, 11, 17
CB 17 MMS	7500	3	1250 ($N_2D^+(3–2)$)	FHSC/young Class 0 protostar	4, 12
SM1N	–	–	100 ($H_2D^+(1_{1,0}–1_{1,1})$)	Prestellar/FHSC/young Class 0 protostar	13,14
Oph A-N6	–	–	700 ($N_2D^+(3–2)$)	Prestellar/FHSC/young Class 0 protostar	13,15
Aqu-MM1	–	–	–	Prestellar/FHSC/young Class 0	4
K242	–	–	–	Prestellar/FHSC/young Class 0	4
MC35-mm	1600	4.2	243[c, d] ($N_2D^+(3–2)$)	FHSC/young Class 0 protostar	18

Notes: (1) This work, (2) Dunham et al. (2011), (3) Enoch et al. (2010), (4) Young et al. (2018), (5) Stephens et al. (2018, 2019), (6) Pineda et al. (2011), (7) Busch et al. (2020), (8) Tsitali et al. (2013), (9) Väisälä et al. (2014), (10) Pezzuto et al. (2012), (11) Hirano & Liu (2014), (12) Chen et al. (2012), (13) Friesen et al. (2018), (14) Friesen et al. (2014), (15) Bourke et al. (2012), (16) Chen et al. (2010), (17) Marcelino et al. (2018), (18) Fujishiro et al. (2020), (19) Hatchell et al. (2007).

[a]Maximum projected values.

[b]Projected distance between the continuum peak and the closest peak of the integrated intensity emission of a deuterated species. The deuterated specie(s) and transition is in parenthesis. If more than one, the average is reported.

[c]Separation is within the beam size of the observation.

[d]Fujishiro et al. (2020) reported no significant difference between the peaks of the $N_2D^+(3–2)$ integrated intensity and the 1.3 mm continuum. The value we report here for the separation corresponds to one-third of the minor axis of their observations.

of the Herschel beam at a wavelength *wv*. The latter correspond to 12, 17, 24, and 35 arcsec for the wavelengths 160, 250, 350, and 500 μm, respectively. Errors were calculated as the sum of the 10 per cent calibration error and the 1σ point source sensitivity taken as 12 mJy for SPIRE measurements and 33 mJy for PACS measurements.[2] The assumed 10 per cent calibration error is a conservative approximation of the combined uncertainty in the flux calibration for point sources (5.5 per cent and 7 per cent for SPIRE and PACS bands, respectively) and an additional (∼4 per cent) uncertainty for extended emission due to uncertainty in the measured beam area (Bendo et al. 2013; Griffin et al. 2013; Balog et al. 2014). Table D2 summarizes the measured fluxes at these wavelengths for Per-bolo 45, Per-bolo 58, and L1451-mm. In addition, only Per-bolo 58 was detected in the PACS band at 70 μm, for which the 1σ point source sensitivity is about 20 mJy. The measured flux for Per-bolo 58 at 70 μm was 0.1 Jy, in agreement with the results of Enoch et al. (2010) based on *Spitzer* observations (∼0.065 Jy).

Table D2. Herschel photometry.

Source	Wavelength (μm)	Flux (Jy)	Flux error (Jy)
Per-bolo 45	160	1.1	0.1
	250	9.5	1.0
	350	6.7	0.7
	500	6.4	0.6
Per-bolo 58	160	1.8	0.2
	250	2.9	0.3
	350	3.2	0.3
	500	1.7	0.2
L1451-mm	160	0.4	0.1
	250	1.5	0.2
	350	2.8	0.3
	500	1.7	0.2

[2]http://herschel.esac.esa.int/Docs/PMODE/html/ch02s03.html

This paper has been typeset from a TEX/LATEX file prepared by the author.